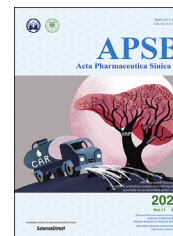




Chinese Pharmaceutical Association  
Institute of Materia Medica, Chinese Academy of Medical Sciences

Acta Pharmaceutica Sinica B

[www.elsevier.com/locate/apsb](http://www.elsevier.com/locate/apsb)  
[www.sciencedirect.com](http://www.sciencedirect.com)



ORIGINAL ARTICLE

# Functional metabolomics reveal the role of AHR/GPR35 mediated kynurenic acid gradient sensing in chemotherapy-induced intestinal damage



Di Wang<sup>a</sup>, Danting Li<sup>a</sup>, Yuxin Zhang<sup>b</sup>, Jie Chen<sup>a</sup>, Ying Zhang<sup>a</sup>,  
Chuyao Liao<sup>a</sup>, Siyuan Qin<sup>a</sup>, Yuan Tian<sup>a</sup>, Zunjian Zhang<sup>a,\*</sup>,  
Fengguo Xu<sup>a,\*</sup>

<sup>a</sup>Key Laboratory of Drug Quality Control and Pharmacovigilance (Ministry of Education), State Key Laboratory of Natural Medicine, China Pharmaceutical University, Nanjing 210009, China

<sup>b</sup>Nanjing Drum Tower Hospital, the Affiliated Hospital of Nanjing University Medical School, Nanjing 210008, China

Received 6 May 2020; received in revised form 14 July 2020; accepted 15 July 2020

**Abbreviations:** 1-MT, 1-methyl-tryptophan; AG, AG490; AHR, aryl hydrocarbon receptor; ARNT, aryl hydrocarbon receptor nuclear translocator; BCA, bicinchoninic acid; BSA, bovine serum albumin; CH, CH223191; CPT-11, irinotecan; CYP1A1, cytochrome P450 1A1; DAI, disease activity index; Dens-Cl, *N*-diethyl-amino naphthalene-1-sulfonyl chloride; DMSO, dimethyl sulfoxide; Dns-Cl, *N*-dimethyl-amino naphthalene-1-sulfonyl chloride; DPP-4, dipeptidyl peptidase-4; DRE, dioxin response elements; DSS, dextran sulphate sodium; ECL, enhanced chemiluminescence; ELISA, enzyme-linked immunosorbent assay; ERK1/2, extracellular regulated protein kinases 1/2; ESI, electrospray ionization; FBS, fetal bovine serum; GE, gastric emptying; GFP, green fluorescence protein; GI, gastrointestinal transit; GPR35, G protein-coupled receptor 35; HE, hematoxylin and eosin; HRP, horseradish peroxidase; IBD, inflammatory bowel disease; IDO1, indoleamine 2,3-dioxygenase 1; IL-6, interleukin-6; IS, internal standard; JAK2, janus kinase 2; KA, kynurenic acid; KAT, kynurenine aminotransferase; KYN, kynurenine; LC-MS, liquid chromatography–mass spectrometry; Linag, linagliptin; LPS, lipopolysaccharides; MOE, molecular operating environment; MOI, multiplicity of infection; MRM, multiple-reaction monitoring; MTT, thiazolyl blue tetrazolium bromide; PBS, phosphate buffer saline; PDB, protein data bank; PDE5, phosphodiesterase type-5; PF, PF-04859989; PMA, phorbol 12-myristate 13-acetate; PMSF, phenylmethylsulfonyl fluoride; RIPA, radioimmunoprecipitation; RPKM, reads per kilobase per million mapped reads; RPMI 1640, Roswell Park Memorial Institute 1640; RT-PCR, real-time polymerase chain reaction; STAT3, signal transducer and activator of transcription 3; Trp, tryptophan; Vard, vardenafil; VCR, vincristine.

\*Corresponding authors. Tel./fax: +86 25 83271454 (Zunjian Zhang), Tel./fax: +86 25 83271021 (Fengguo Xu).

E-mail addresses: [fengguoxu@cpu.edu.cn](mailto:fengguoxu@cpu.edu.cn) (Fengguo Xu), [zunjianzhangcpu@hotmail.com](mailto:zunjianzhangcpu@hotmail.com) (Zunjian Zhang).

Peer review under responsibility of Chinese Pharmaceutical Association and Institute of Materia Medica, Chinese Academy of Medical Sciences.

<https://doi.org/10.1016/j.apsb.2020.07.017>

2211-3835 © 2021 Chinese Pharmaceutical Association and Institute of Materia Medica, Chinese Academy of Medical Sciences. Production and hosting by Elsevier B.V. This is an open access article under the CC BY-NC-ND license (<http://creativecommons.org/licenses/by-nc-nd/4.0/>).

## KEY WORDS

Intestinal toxicity;  
Kynurenine pathway;  
Gradually sensing;  
AHR;  
GPR35

**Abstract** Intestinal toxicity induced by chemotherapeutics has become an important reason for the interruption of therapy and withdrawal of approved agents. In this study, we demonstrated that chemotherapeutics-induced intestinal damage were commonly characterized by the sharp upregulation of tryptophan (Trp)–kynurenine (KYN)–kynurenic acid (KA) axis metabolism. Mechanistically, chemotherapy-induced intestinal damage triggered the formation of an interleukin-6 (IL-6)–indoleamine 2,3-dioxygenase 1 (IDO1)–aryl hydrocarbon receptor (AHR) positive feedback loop, which accelerated kynurenine pathway metabolism in gut. Besides, AHR and G protein-coupled receptor 35 (GPR35) negative feedback regulates intestinal damage and inflammation to maintain intestinal integrity and homeostasis through gradually sensing kynurenic acid level in gut and macrophage, respectively. Moreover, based on virtual screening and biological verification, vardenafil and linagliptin as GPR35 and AHR agonists respectively were discovered from 2388 approved drugs. Importantly, the results that vardenafil and linagliptin significantly alleviated chemotherapy-induced intestinal toxicity *in vivo* suggests that chemotherapeutics combined with the two could be a promising therapeutic strategy for cancer patients in clinic. This work highlights GPR35 and AHR as the guardian of kynurenine pathway metabolism and core component of defense responses against intestinal damage.

© 2021 Chinese Pharmaceutical Association and Institute of Materia Medica, Chinese Academy of Medical Sciences. Production and hosting by Elsevier B.V. This is an open access article under the CC BY-NC-ND license (<http://creativecommons.org/licenses/by-nc-nd/4.0/>).

## 1. Introduction

Chemotherapy is still the main treatment for cancers. However, chemotherapeutics are always accompanied with intestinal adverse reactions including diarrhea, constipation and peptic ulcer due to their non-selection, megadose and long-course, which eventually lead to vicious malnutrition and cachexia, even shock and death<sup>1–3</sup>. It was reported that over 40% of chemotherapy patients suffer from intestinal toxicity in clinic, which has become an important reason for the interruption of therapy or withdrawal of approved chemotherapy agents<sup>4–6</sup>. However, unfortunately, there remains lack of clinically effective intervention targets and approach for the chemotherapeutics-induced intestinal injury<sup>7,8</sup>.

Metabolites contain the ultimate interactive information of genome, transcriptome and proteome, and directly reflect the characteristics of disease and external stimuli phenotypes<sup>9,10</sup>. Our previous studies showed that intestinal damage induced by chemotherapeutics severely disrupted multiple nutrient metabolisms, including tryptophan<sup>11–13</sup>. Tryptophan (Trp) and its metabolites play key roles in diverse physiological processes ranging from cell growth and coordination of organismal responses to the environment and dietary<sup>14,15</sup>. Noteworthy, over 95% of the free Trp is degraded through the kynurenine (KYN) pathway which plays key roles in the regulation of immunity, neuronal function and intestinal homeostasis<sup>15,16</sup>. The expanding knowledge on key functions of Trp metabolism has revealed a number of therapeutic strategies, mainly focusing on the development of IDO (the key enzyme of catalyzing Trp to KYN) inhibitors in immuno-oncology<sup>17</sup>. However, the increasing failures of clinical trials with IDO inhibitors for the additional undesirable symptoms, including intestinal toxicity, rise a question regarding whether complete blockade of Trp catabolism to KYN pathway may elicit tolerability<sup>18,19</sup>. Ultimately, a lack of clear understanding of the specific downstream effector mechanism of Trp metabolism is the major obstacle in drug development<sup>16</sup>.

In the central nervous system, the KYN pathway carries out its physiological functions through *N*-methyl-daspartate receptor

(NMDAR) and  $\alpha 7$  nicotinicacetylcholine receptor ( $\alpha 7$ nAChR), while in peripheral tissues, aryl hydrocarbon receptor (AHR) and GPR35 are its primary mediator<sup>15,16</sup>. AHR plays important roles in various physiological processes, such as epithelial barrier function, cell homeostasis and immune responses<sup>20,21</sup>. Although KYN and kynurenic acid (KA), the main metabolites of the KYN pathway, as AHR endogenous ligands, have been reported earlier, they have not received adequate attention, as studies increasingly focus on the role of AHR in microbial metabolism<sup>22,23</sup>. Besides, GPR35, an orphan receptor discovered in 1998, is highly expressed in gastrointestinal tract and plays various physiological functions through binding to KA<sup>24,25</sup>. Currently, the identification of GPR35 polymorphisms as a risk factor associated with inflammatory bowel disease (IBD) suggests that GPR35 is crucial in maintaining intestinal homeostasis, nevertheless relatively little is known about GPR35<sup>26</sup>. Interestingly, we found that different chemotherapeutics-induced intestinal damage was commonly characterized by the up-regulation of KYN metabolic pathway in our preliminary experiments. The current pharmacological research has demonstrated that AHR and GPR35 play indispensable and nonoverlapping roles in mediating metabolite functions<sup>15</sup>. However, as the dual-sensor of the KYN metabolic pathway, their potential interrelation in regulating intestinal damage and repair remains enigmatic.

Here, we use functional metabolomics approaches to explore the mechanism of occurrence and development of chemotherapy-induced intestinal toxicity and seek effective therapies. Our study demonstrates that AHR and GPR35 mediate and repair intestinal damage with a KA gradient sensing mode. Because of sensitivity difference of AHR and GPR35 with KA, colon tissue primarily formed an IL-6–IDO1–AHR positive feedback regulation loop to accelerate KYN and KA accumulation at the early stage of intestinal damage. Simultaneously, with the accumulation of KA, GPR35 negative feedback regulates intestinal injury to promote colon repair and maintain intestinal homeostasis through sensing KA level selectively. More importantly, GPR35 and AHR agonists were screened and identified from 2388 approved drugs, which

proved to be a promising intervention strategy for the intestinal toxicity of chemotherapy in clinic.

This study has two main objectives. The first is to study the mechanisms of Trp–KYN–KA axis in drug-induced intestinal damage and self-repair using the functional metabolomics method. The second is to discover new applications in alleviating drug-induced intestinal damage from approved drugs based on the functional mechanism studies. In order to investigate the change of tryptophan metabolism profile in drug-induced intestinal damage, we firstly constructed vincristine (VCR)-induced rat ileus, irinotecan (CPT-11)-induced rat diarrhea and dextran sulphate sodium (DSS)-induced rat inflammatory bowel disease (IBD) models, and the metabolites of colon tissue were quantified by LC–MS/MS using twin-derivatization method. Human colonic epithelial cells (NCM460 cell line) were used to detect the effects of KYN and KA on wound healing, receptor internalization, mRNA and protein expression, and co-culture of NCM460 and THP-1 cells were used to simulate colon inflammation *in vitro*. Subsequently, GPR35 and AHR agonists were discovered from 2388 approved drugs through virtual screening, clinical data analysis and biological verification. Simultaneously, the pharmacodynamic evaluation *in vivo* was performed on irinotecan-induced rat diarrhea model. All cellular experiments were conducted in triplicates independently, unless otherwise noted. Rats were randomly assigned to control and treatment groups, no blinding was carried out during experimental administration, and no bias was performed during husbandry, diarrhea scoring and tissue harvesting.

## 2. Materials and methods

### 2.1. Cell culture and co-culture

THP-1 cell line was obtained from American Type Culture Collection (Manassas, VA, USA), and cultured in Roswell Park Memorial Institute (RPMI) 1640 medium (Gibco, Grand Island, NY, USA) supplemented with 10% fetal bovine serum FBS (Gibco) and 1 × HEPES buffer (Boster, Wuhan, China). NCM460 cell line was obtained from Nanjing Hongxin Biological Technology Co. Ltd. (Nanjing, China), and cultured in RPMI 1640 medium supplemented with 10% FBS and 1 mmol/L penicillin–streptomycin. All cells were maintained at 37 °C in a humidified atmosphere containing 5% CO<sub>2</sub>. All cells were identified at Shanghai Biowing Biotechnology Co. Ltd. (Shanghai, China), sample codes were 20190122-01 and 20190625-01, respectively.

THP-1 monocytes (1 × 10<sup>6</sup> cells/well) were seeded into the upper chamber of 6-well transwell plate (0.4 μm pore size; Corning, MA, USA), stimulated to differentiate into macrophages by 100 ng/mL phorbol 12-myristate 13-acetate (PMA; Sigma, St. Louis, MO, USA) for 48 h, followed by culturing with 1 μg/mL lipopolysaccharides (LPS; Sigma) for 24 h. Simultaneously, NCM460 cells (5 × 10<sup>5</sup> cells/well) were seeded into the lower chamber to allow cells adherence to the walls. Then, the chambers with THP-1-derived macrophages were placed directly on top of six-well plates containing the NCM460 cells. NCM460 cells and the supernatant were collected after co-culture systems were treated with KA and KYN for 48 h for real-time PCR, Western blotting and enzyme-linked immunosorbent assays (ELISA).

### 2.2. Cell viability and intestinal epithelial cell migration assays

Cells were seeded into 96-well plates with 5 × 10<sup>3</sup> cells/well and adhered overnight. After vehicle and test compounds treatment for 48 h, 20 μL/well of MTT (5 mg/mL) was added and incubated for another 4 h at 37 °C. Then, DMSO dissolved purple formazan crystals, and the absorbance was measured at 490 nm by a microplate reader (Tecan, Mannedorf, Switzerland).

Colonic epithelial cells (1 × 10<sup>5</sup> cells/well) were plated in 24-well plate, and maintained until the cells reached 90%–100% confluent. Subsequently, a straight scratch across the cells monolayer was made using a sterile 20 μL pipette tip, and damaged cells were removed by washing with PBS. The images of migrating epithelial monolayers at the same spot were captured with an inverted microscope (Nikon TS100, Tokyo, Japan) after test compound and vehicle treatment for 0, 24 and 48 h. The relative migration (%) was calculated according to the following Eq. (1):

$$\text{Relative migration rate (\%)} = (\text{Wound area}_{0\text{ h}} - \text{Wound area}_{24\text{ or }48\text{ h}}) / \text{Wound area}_{0\text{ h}} \times 100 \quad (1)$$

### 2.3. Receptor internalization analysis

The quantification of receptor internalization was performed by measuring specific antibody-tagged receptor on cells surface using flow cytometry. NCM460 cells were seeded into 6-well plates (2 × 10<sup>5</sup> cells/well) and maintained overnight. Cells were collected and washed with ice-cold PBS by centrifugation after test compounds and vehicle treatment for 48 h. Afterwards, cells of drug treatment groups were incubated with anti-GPR35 antibody (1:300, Proteintech, Chicago, IL, USA) and the negative control was incubated with 3% BSA/PBS buffer at 4 °C for 1 h, followed by all group cells were incubated with secondary antibodies Alexa Fluor® 488 conjugate anti-rabbit IgG (H + L) (1:300, CST, Boston, MA, USA) in 3% BSA/PBS buffer at 4 °C for 45 min after cells were washed twice with ice-cold PBS. Finally, cells were washed twice with ice-cold PBS and resuspended with 1% formaldehyde. Fluorescence intensity of 2 × 10<sup>4</sup> cells for each sample was measured using FACSCalibur instrument (BD Biosciences, San Jose, CA, USA). The percentage of internalized receptor was calculated from surface receptor fluorescence values (*F*) as following Eq. (2):

$$\text{Receptor internalization rate (\%)} = (F_{\text{Control group}} - F_{\text{Drug group}}) / (F_{\text{Control group}} - F_{\text{Negative group}}) \times 100 \quad (2)$$

### 2.4. Construction of stably silenced GPR35 and AHR gene cell lines with shRNA

The human *GPR35* and *AHR* gene silencing lentivirus was constructed and purchased from Shanghai GenePharma Co., Ltd. (Shanghai, China), OrderID: LV2018-15661 and LV2019-14486, and the oligonucleotide sequences are list in [Supporting Information Table S1](#). The lentiviral vector system contains green fluorescence protein (GFP) and puromycin resistance genes, which can be used to screen the infected cells.

Adhered NCM460 cells with 40%–50% confluent and THP-1 cells (3 × 10<sup>5</sup> cells/mL) in 25 cm<sup>2</sup> flask were transfected with lentivirus at a multiplicity of infection (MOI) of 100, and

incubated with RPMI1640 culture medium containing 10% FBS (Gibco), 5 µg/mL polybrene (Sigma). Three days after infection, the medium was replaced with fresh culture medium containing 2 µg/mL puromycin (Sigma), which was changed every 2 days and terminated when the uninfected cells were completely dead. GFP positive cells were observed under a fluorescence microscope (Nikon TS100) and the silencing extent of target gene was analyzed by Western blot.

### 2.5. Enzyme-linked immunosorbent assay

To quantify the levels of IL-6, IL-1 $\beta$ , TNF- $\alpha$  in culture supernatants, serum and colon tissue homogenates, ELISA was performed according to the manufacturer's instructions (4A Biotech Co., Ltd., Beijing, China).

### 2.6. Homology modeling

Homology modeling was conducted in Molecular Operating Environment (MOE, Chemical Computing Group Inc., Montreal, Canada) v2018.0101. Template crystal structures of GPR35 and AHR were identified through BLAST sequence alignment and downloaded from RCSB Protein Data Bank (PDB ID were 5XSZ and 5SY7, respectively). According to reports of the active binding sites of GPR35 and AHR<sup>27,28</sup>, the protonation state of the protein and orientation of the hydrogens were optimized by LigX at the pH value of seven and the temperature of 300 K. First, the target sequence was aligned to the template sequence, and ten independent intermediate models were built. These different homology models were the results of the permutational selection of different loop candidates and side chain rotamers. Then, the intermediate model which scored best according to the GB/VI scoring function was chosen as the final model, and was subjected to further energy minimization using the AMBER10: EHT force field.

### 2.7. Virtual screening

The dock module in MOE was used for virtual screening. The homology model of AHR and GPR35 were defined as receptors and the approved drugs in DrugBank Database (approximately 2388 downloadable molecules at the date of Nov, 2018) as VS library. According to the "Lipinski's rule of five"<sup>29</sup>, the drugs with molecular weight more than 500 or less than 100, and the crystal water and metal salt ions of complexes were removed. Prior to docking, the force field of AMBER10:EHT and the implicit solvation model of Reaction Field (R-field) were selected. The protonation state of the protein and the orientation of the hydrogens were optimized by LigX module at the pH value of 7 and temperature of 300 K. The docking workflow followed the "induced fit" protocol, in which the side chains of the receptor pocket were allowed to move according to ligand conformations, with a constraint on their positions. The weight used for tethering side chain atoms to their original positions was 10. For each ligand, all docked poses were ranked by London dG scoring first, then a force field refinement was carried out on the top 10 poses followed by a rescoring of GBVI/WSA dG.

### 2.8. Animal experiments and sample collection

All animal studies and procedures were conducted in accordance with the US National Institutes of Health Guide for the Care and Use of Laboratory animals and approved by the Animal Ethics

Committee of China Pharmaceutical University (License No: SYXK 2018-0019). Male Sprague–Dawley (SD) rats at the age of 6–8 weeks were purchased from Vital River Laboratory Animal Technology Co., Ltd. (Pinghu, China), permit Nos. SCXK (Zhe) 2018-0001 and SCXK (Zhe) 2019-0001, respectively. All rats were housed in a temperature-controlled environment (24  $\pm$  2 °C) for a week acclimation with a standard rodent diet under 12 h/12 h dark/light cycle before the experiments started.

#### 2.8.1. Vincristine-induced ileus model

The treatments and procedures of rat experiments were performed as previous report of our laboratory<sup>30</sup>. Briefly, after acclimatization, 32 SD rats were randomly divided into two groups ( $n = 16$ ). Model group rats were administrated with VCR (0.2 mg/kg; Zhejiang Hisun Chemical Co., Ltd., Zhoushan, China) by intravenous injection once every two days for eight days, and control group rats were injected with the equivalent of saline simultaneously. The body weight were measured every day. Eight rats in each group were subjected to phenol red gelatin to verify the histological progress of paralytic ileus by investigating the changes of rats gastric emptying (GE) and gastrointestinal transit (GI) according to the previous description<sup>31</sup>. On Day 9 after blood samples were obtained from the orbital venous plexus, rats were sacrificed and colon tissues were collected.

#### 2.8.2. Irinotecan-induced diarrhea model

CPT-11 was obtained as irinotecan hydrochloride (Jaripharm, Lianyungang, China) and its injection was prepared according to literature<sup>32</sup>. After acclimatization, 16 SD rats were randomly divided into two groups (control group  $n = 9$ , model group  $n = 7$ ). Model group rats were administered with CPT-11 intravenously at the dosage of 150 mg/kg once a day for two consecutive days, control group rats were injected with the equivalent of vehicle simultaneously. Body weight and diarrhea score of every individual were monitored twice every day. Diarrhea score was assessed according to the previous reports<sup>33</sup>. Blood and colon tissue samples were collected on Day 5, the most severe day of the late-onset diarrhea.

#### 2.8.3. Dextran sulphate sodium-induced IBD model

After acclimatization, 16 SD rats were randomly divided into two groups ( $n = 8$ ). Model group rats were administered with 5% ( $w/v$ ) DSS (MW = 40 kDa; Aladdin, Shanghai, China) solution in drinking water for 9 consecutive days, and control group were received normal drinking water. Body weight and disease activity index (DAI) were recorded daily. The DAI was determined by combining the scores for body weight loss, stool consistency and gross bleeding according to the previous reports<sup>34,35</sup>. On Day 9 after blood samples were obtained from the orbital venous plexus, rats were sacrificed and colon tissues were collected.

#### 2.8.4. Vardenafil and linagliptin intervention in drug-induced intestinal damage

After acclimatization, 50 SD rats were randomly divided into five groups ( $n = 10$ ). Model group rats were intragastrically administered with the equivalent of saline for 7 consecutive days, and intravenously injected with CPT-11 at the dosage of 120 mg/kg each day for two consecutive days on Day 3. For the three drug intervention groups, rats were intragastrically administered with vardenafil (Vard, 10 mg/kg), linagliptin (Linag, 3 mg/kg) and Vard + Linag (10 and 3 mg/kg) respectively for 7 consecutive days and CPT-11 treatment was the same as the model group. Control group rats were

intra-gastrically administered with saline and intravenously injected with vehicle as model group. As described above, body weight and diarrhea score were monitored twice daily. Simultaneously, blood and colon tissue samples were collected on Day 7.

All blood samples were centrifuged at 8000 rpm (Centrifuge 5430 R, Eppendorf, Hamburg, Germany) for 10 min after coagulation for 1 h, then serum samples were aliquoted and stored at  $-80^{\circ}\text{C}$  until preparation and analysis. For every colon tissue sample, a portion were fixed in 10% formalin for histological examination and the rest were stored at  $-80^{\circ}\text{C}$  for Western blot, metabolomics and ELISA analysis.

## 2.9. LC-MS/MS quantify metabolite

### 2.9.1. Sample preparation and twin derivatization

For cell samples, cells were seeded into 10-cm dish, setting parallel groups for normalization using BCA protein assay kit according to the manufacturer's instructions. After treatment, cells were quenched with 3 mL cold methanol/ $\text{H}_2\text{O}$  (80:20, v/v) at  $-80^{\circ}\text{C}$  for 10 min, followed by scraping and transference into a tube. Cell suspension was subjected to vortex and ultrasonication thrice at 100 W for 5 min on ice, then the supernatant was collected after centrifugation (12,000 rpm, 10 min,  $4^{\circ}\text{C}$ ; Eppendorf) and evaporated to dryness at  $37^{\circ}\text{C}$  under nitrogen for further derivatization. For rat samples, about 50 mg of each colon tissue sample was homogenized with precooled saline (1:5, w/v) using a tissue homogenizer. Methanol was added to 50  $\mu\text{L}$  tissue homogenate (10:1, v/v), then the mixture was vortexed for 10 min to precipitate protein and extract metabolites. All supernatant was collected after centrifugation (12,000 rpm, 10 min,  $4^{\circ}\text{C}$ ; Eppendorf) and evaporated to dryness at  $37^{\circ}\text{C}$  under nitrogen for further derivatization. Meanwhile, to construct calibration curve, ten concentration levels of each metabolite were prepared using their standards (Supporting Information Tables S2 and S3). Blank biological substrates (charcoal-treated colon homogenates and extracting solution of cells) 50  $\mu\text{L}$  was added to 100  $\mu\text{L}$  corresponding standard solution, then the protein precipitation, metabolite extraction and dryness were the same as the rat sample preparation.

Samples derivatization was performed according to our previous study<sup>13</sup>, with a slight modification. The desiccated samples were dissolved in 100  $\mu\text{L}$   $\text{Na}_2\text{CO}_3$ - $\text{NaHCO}_3$  buffer (pH = 10.5) and reacted with 100  $\mu\text{L}$  Dns-Cl (3 mg/mL; Sigma) at  $60^{\circ}\text{C}$  for 60 min. Internal standard (IS) solution was prepared by labeling nitrogen dried standards mixture (10  $\mu\text{g}/\text{mL}$  Trp, 200 ng/mL KA, 100 ng/mL KYN for rat samples; 1000 ng/mL Trp, 500 ng/mL KA, 500 ng/mL KYN for cell samples) with Dens-Cl solution (100  $\mu\text{L}$ , 5 mg/mL) (synthesized by our laboratory according to Ref. 13) and carbonate buffer (100  $\mu\text{L}$ , pH = 11.5) incubated at  $60^{\circ}\text{C}$  for 60 min. After cooling, the samples were spiked with 10  $\mu\text{L}$  IS and extracted with one mL ethyl acetate by vortex for 10 min, centrifugation for 10 min in 8000 rpm (Eppendorf) and the ethyl acetate (upper) layer was collected. Then samples were dissolved in 100  $\mu\text{L}$  mobile phase (MeOH, 10 mmol/L;  $\text{NH}_4\text{AC}$ , 40/60) after evaporation by nitrogen at  $37^{\circ}\text{C}$ . Samples was injected into the LC system by autosampler and analyzed with LC-MS/MS. All manipulations were performed under a lucifuge environment.

### 2.9.2. LC-MS/MS analysis

Chromatography separation was performed on a C18 Column (50 mm  $\times$  2.1 mm, 2.2  $\mu\text{m}$ ; Phenomenex Gemini, Torrance, CA, USA) and the gradient program was set as follows with solvent A

(10 mmol/L  $\text{NH}_4\text{AC}$ ) and solvent B (MeOH): 0–6 min 40%–80% B, 6–10 min 80% B, and 10–15 min 40% B. The injection volume was 5  $\mu\text{L}$  and flow rate was 0.3 mL/min. The mass spectrometry analysis was performed on a triple quadruple TSQ Quantum mass spectrometer with ESI source (Thermo Fisher, Palo Alto, CA, USA), and the parameters were set as follows: ESI<sup>+</sup>, spray voltage 4.5 kV, capillary temperature  $250^{\circ}\text{C}$ , scan width for multiple-reaction monitoring (MRM) 0.2  $m/z$ , sheath gas pressure 30 arb ( $\text{N}_2$ ), aux gas pressure 7 arb ( $\text{N}_2$ ). Precursor ion and product ion scan were performed in the automatic MS/MS synchronized survey scan mode for structural confirmation. The main parameters for MS/MS detection of each analyte were summarized in Supporting Information Table S4.

### 2.9.3. Data analysis

The original LC-MS/MS data were processed by Xcalibur 3.0 software (Thermo Fisher) for peak detection and alignment. The primary parameters were set as follows: retention time window, 0.5 min; integration smoothing points, 5; baseline window, 40; area noise factor, 5; peak noise factor, 10. Other parameters were set as default. A resulting matrix consisting of peak area was generated and exported to an excel table. Calibration curves were constructed by plotting the peak–area ratio of each metabolite to its corresponding IS versus the concentrations of the metabolite in each corresponding matrix. Then, the concentrations of metabolites in each sample were calculated by their corresponding calibration curve (Supporting Information Table S5). The metabolite concentrations in the cell sample were normalized by quantifying total cell protein, and metabolite concentrations in the colon sample were normalized by tissue weight.

## 2.10. mRNA preparation and quantitative real-time RT-PCR

Total RNA was extracted from cells using RNAiso Plus (TaKaRa Biotechnology, Dalian, China) according to the manufacturer's instructions. The RNA concentration was detected using NanoDrop 2000 (Thermo Fisher Scientific, Waltham, MA, USA), and then 1  $\mu\text{g}$  total RNA was reverse transcribed to complementary DNA (cDNA) using PrimeScript<sup>TM</sup> RT reagent Kit (TaKaRa) according to the manufacturer's instructions. Subsequently, qRT-PCR was performed using SYBR Green I Master (Roche Diagnostics, Basel, Switzerland) on a LightCycler 480 instrument (Roche) following the manufacturer's instructions. The relative expression levels of target genes were calculated by the  $2^{-\Delta\Delta\text{CT}}$  method, and normalized by  $\beta$ -actin in each sample. The primers used in qRT-PCR are listed in Supporting Information Table S6.

## 2.11. Western blotting

Cells and tissues were lysed by radioimmunoprecipitation (RIPA) buffer (Beyotime Biotechnology, Shanghai, China) containing 1 mmol/L phenylmethylsulfonyl fluoride (PMSF, Thermo Fisher Scientific) on ice vortexed every 5 min for 30 min or homogenized by a tissue homogenizer (Bioprep-24 homogenizer, Hangzhou, China). The lysates were centrifuged at  $12,000\times g$  for 15 min at  $4^{\circ}\text{C}$ , and then the protein concentrations of supernatants were measured using a BCA protein assay kit (Thermo Fisher Scientific), followed by the lysates were supplemented with sample loading buffer (Beyotime Biotechnology) and denatured at  $95^{\circ}\text{C}$  for 10 min. Proteins (30  $\mu\text{g}$ ) were separated by SDS–polyacrylamide gel electrophoresis on 8%–15% gel and transferred to polyvinylidene difluoride membranes (0.2  $\mu\text{m}$ ,

Millipore, MA, USA) using an electroblotting apparatus (Tanon Science & Technology, Shanghai, China). The membranes were blocked with 5% milk in PBS containing 0.1% Tween 20 (PBST) for 2 h at room temperature and incubated with primary antibodies (listed in [Supporting Information Table S7](#)) at 4 °C overnight. After washed 3 times with PBST, the membranes were subjected to secondary antibody conjugated to horseradish peroxidase (HRP; Proteintech) for approximately 2 h at room temperature. Then, the immunoreactive bands were visualized using an enhanced chemiluminescence (ECL) system (Millipore) on a Tanon 5200 chemiluminescent imaging system (Tanon Science & Technology). Relative protein expression was calculated by densitometric analysis using ImageJ software.

### 2.12. Immunohistochemistry and hematoxylin and eosin (HE) staining

Colon tissues were fixed in 10% buffered formalin for 3 days, embedded in paraffin and then sectioned at a thickness of 4  $\mu$ m. Sections were either subjected to HE staining or performed immunohistochemistry. For HE staining, the sections were prepared orderly by dewaxing with graded xylene and ethanols, staining with HE solution, then dehydrating and mounting with neutral resin. For immunohistochemistry, the sections were subjected to deparaffinization, antigen retrieval and blocking with goat serum, followed by incubating with anti-CD68 or anti-iNOS rabbit polyclonal antibodies (Servicebio, Wuhan, China) overnight at 4 °C. After washed with PBS, the sections were incubated with HRP-conjugated goat anti-rabbit IgG secondary antibody (Invitrogen, Carlsbad, CA, USA) and the peroxidase reaction was developed with diaminobenzidine (Dako, Copenhagen, Denmark). Subsequently, the sections were counterstained with hematoxylin, and the images were captured using an inverted microscope.

The key material and resources used in all experiment are listed in [Table S7](#).

### 2.13. Statistical analysis

Graphpad Prism 6.0 Software (GraphPad Software Inc., La Jolla, CA, USA) was used for all statistical analyses. All experiments were duplicated at least three times, and the results were presented as mean  $\pm$  standard deviation (SD), unless otherwise specified. Statistical analysis of cells migration were performed at the 48 h point. Independent unpaired two-tailed Student's *t* test was performed to evaluate the differences between two groups. Multiple group comparisons were analyzed using one-way analysis of variance (ANOVA) with Bonferroni correction. A value of  $P < 0.05$  was considered statistically significant.

## 3. Results

### 3.1. Chemotherapy-induced intestinal damage interrupts tryptophan metabolism

Considerable studies have shown that tryptophan and its metabolites play a vital role in maintaining intestinal homeostasis<sup>36</sup>. To explore the change of tryptophan metabolism profile in chemotherapy-induced intestinal toxicity, we constructed vincristine-induced rat ileus model and irinotecan-induced rat diarrhea model in this study. The results of rat body weight reduction, gastric emptying and gastrointestinal transit

suppression, diarrhea score increase and histopathological changes after drugs administration demonstrated that rats suffered severe intestinal toxicity, and their gut were significantly damaged ([Supporting Information Fig. S1A and S1B](#)). Then, we quantified the KYN pathway of tryptophan metabolism based on the targeted metabolomics analysis ([Fig. 1A](#)). We found that the levels of KYN and KA in the colon were sharply raised after the chemotherapeutics administration, and the fold change were 3–4 and 12–15, respectively ([Fig. 1B](#)). These results indicate KYN and KA dramatically accumulated in damaged gut.

To further explore whether this phenomena is a common feature, we subsequently constructed dextran sulphate sodium-induced rat IBD model ([Fig. S1C](#)), which is the most widely used among experimental models of chemically induced intestinal damage. Interestingly, KYN and KA levels in colon were also significantly elevated in DSS-induced intestinal damage ([Fig. S1D](#)). Collectively, the same change profile in the three models suggests that the up-regulation of Trp–KYN–KA axis metabolism in damaged gut was commonly characterized by diverse chemotherapeutics. To further determinate the change of KYN pathway, we analyzed the KYN/Trp ratio which was frequently used to reflect the activity of IDO. The results show that KYN/Trp ratio was inordinately increased in all three intestinal damage models ([Fig. 1C](#)), indicating that the IDO activity or expression was promoted. These results demonstrate that intestinal damage leads to the acceleration of Trp catabolism *via* the KYN pathway.

### 3.2. Trp–KYN–KA axis plays an important role in colon cell wound healing

Our previous studies found that damaged gut induced by CPT-11<sup>12</sup> and VCR respectively was significantly recovered after termination of drug treatment, hypothesizing that there is a mechanism of intestinal repair. However, the rationale remains enigmatic. Currently, although the KYN metabolic pathway exhibits a fascinating potential in various physiological and pathological processes such as energy homeostasis, mental health and immune response<sup>15</sup>, little is known about the role of Trp–KYN–KA metabolic axis plays in drug-induced intestinal injury and repair.

Thus, we firstly researched the effects of KYN and KA on the migration of monolayer colonic epithelial cell which is the essential physiological process for tissue repair and homeostasis. The results show that KYN and KA significantly promoted the wound healing of human colonic epithelial cells ([Fig. 1D](#); [Supporting Information Fig. S2A and S2B](#)), suggesting that Trp–KYN–KA axis plays an important role in maintaining intestinal integrity, at least partially. Naturally, these results make us deeply interested in the rationale of KYN and KA accumulation in damaged gut. Subsequently, we found that the level of IL-6 in colon was dramatically elevated after rats were administrated with VCR, CPT-11 and DSS ([Fig. S2C](#)). These results suggest that the occurrence of tissue inflammation is possibly related to the accumulation of KYN and KA in damaged gut. After treated with IL-6, the KYN and KA level in NCM460 cells was observably raised ([Fig. 1E](#)), which verified our supposition. In this case, we detected the effect of IL-6 on cell migration, and found that IL-6 also significantly promoted wound healing of NCM460 cells ([Fig. 1F and Fig. S2D](#)). To further reveal the relationship between IL-6 and Trp–KYN–KA axis, we suppressed KYN metabolic pathway using an IDO1 inhibitor 1-methyl-tryptophan (1-MT; [Fig. S2E](#)). As the result demonstrates that the wound healing

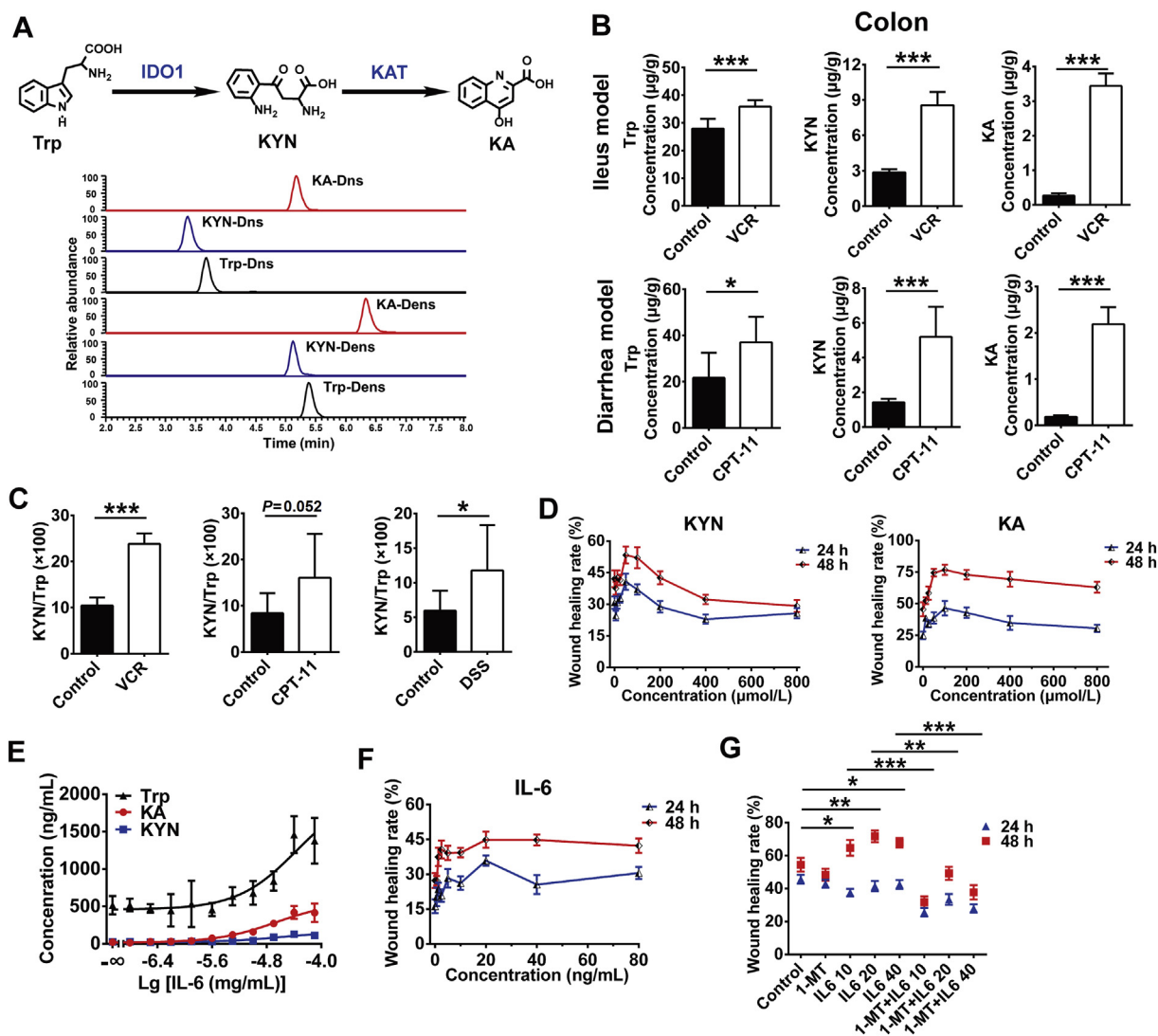


**Figure 1** Trp–KYN–KA axis plays an important role in colon cell wound healing. (A) Schematic diagram of Trp–KYN–KA metabolic axis (upper panel). L-Trp, tryptophan; KYN, kynurenine; KA, kynurenic acid; IDO1, indoleamine 2,3-dioxygenase 1; KAT, kynurenine aminotransferase. The representative LC–MS/MS chromatogram of Trp, KYN and KA derivatives and their corresponding internal standards (under panel). (B) LC–MS/MS quantitative analysis of Trp, KYN and KA concentrations in the colon of VCR-induced ileus and CPT-11-induced diarrhea model rats ( $n = 6–9$ ). (C) The KYN/Trp ratio in rat colon used to reflect IDO1 activity ( $n = 6–9$ ). (D) Quantitative analysis of the migration changes of monolayer NCM460 cells after KYN and KA treatment for 24 and 48 h, showing wound healing rate as compared with initial scratch size ( $n = 3$ ). (E) LC–MS/MS quantitative analysis of the metabolic changes of Trp, KYN and KA in NCM460 cells after IL-6 treatment for 48 h ( $n = 3$ ). (F) Quantitative analysis of the effect of IL-6 on monolayer NCM460 cell migration ( $n = 3$ ). (G) Quantitative analysis of the effect of IDO1 inhibitor 1-MT (0.5 mmol/L) on NCM460 cell migration induced by IL-6 ( $n = 3$ ). Data are presented as mean  $\pm$  SD. Statistical analysis was performed using Student's *t* test. \* $P < 0.05$ , \*\* $P < 0.01$  and \*\*\* $P < 0.001$ .

promoted by IL-6 was markedly inhibited by 1-MT (Fig. 1G and Fig. S2F). Taken together, our findings illuminate that IL-6 promoted intestinal cell migration through accelerating the metabolism of Trp–KYN–KA axis.

### 3.3. AHR positive feedback regulates KYN pathway metabolism through sensing KYN and KA levels in gut

The environmental sensor AHR is widely expressed in various tissues, especially in barrier systems such as the gut. Despite the fact that AHR was initially described as a receptor for dioxin and other xenobiotics, it is clear that AHR serves to drive a variety of important physiological functions through sensing its endogenic

ligands<sup>22</sup>. In the following study, we demonstrate that AHR was activated by KYN and KA through detecting the expression of cytochrome P450 1A1 (CYP1A1; Supporting Information Fig. S3A) which is an AHR target gene. Interestingly, KYN and KA significantly promoted IL-6 protein and mRNA expression in NCM460 cells, and the effects were dramatically inhibited when AHR response was blocked by its specific inhibitor CH223191 (Fig. S3B and S3C). These results suggest that AHR mediates IL-6 expression in intestinal epithelial cells through sensing KYN and KA. To further confirm this hypothesis, we firstly analyzed the AHR response element in the *IL-6* gene promoter regions based on eukaryotic promoter database. As the results shown in Fig. S3D, there is at least one binding site of AHR heterodimer (AHR:ARNT,

AHR heterodimerization with ARNT and binding to DRE sequences of the target gene promoter to regulate transcription<sup>37</sup>) in the promoter regions of the human *IL-6* gene. Subsequently, we performed knockdown of *AHR* expression (Fig. 2A). Consistently, the results show that the increase of IL-6 protein and mRNA

expression induced by KYN and KA was significantly inhibited after the *AHR* gene was silenced (Fig. 2A and B).

Since KA is a metabolite of KYN catalyzed by kynurenine aminotransferase (KAT), we next clarified whether there is a difference in AHR sensibility in response to KYN and KA levels.

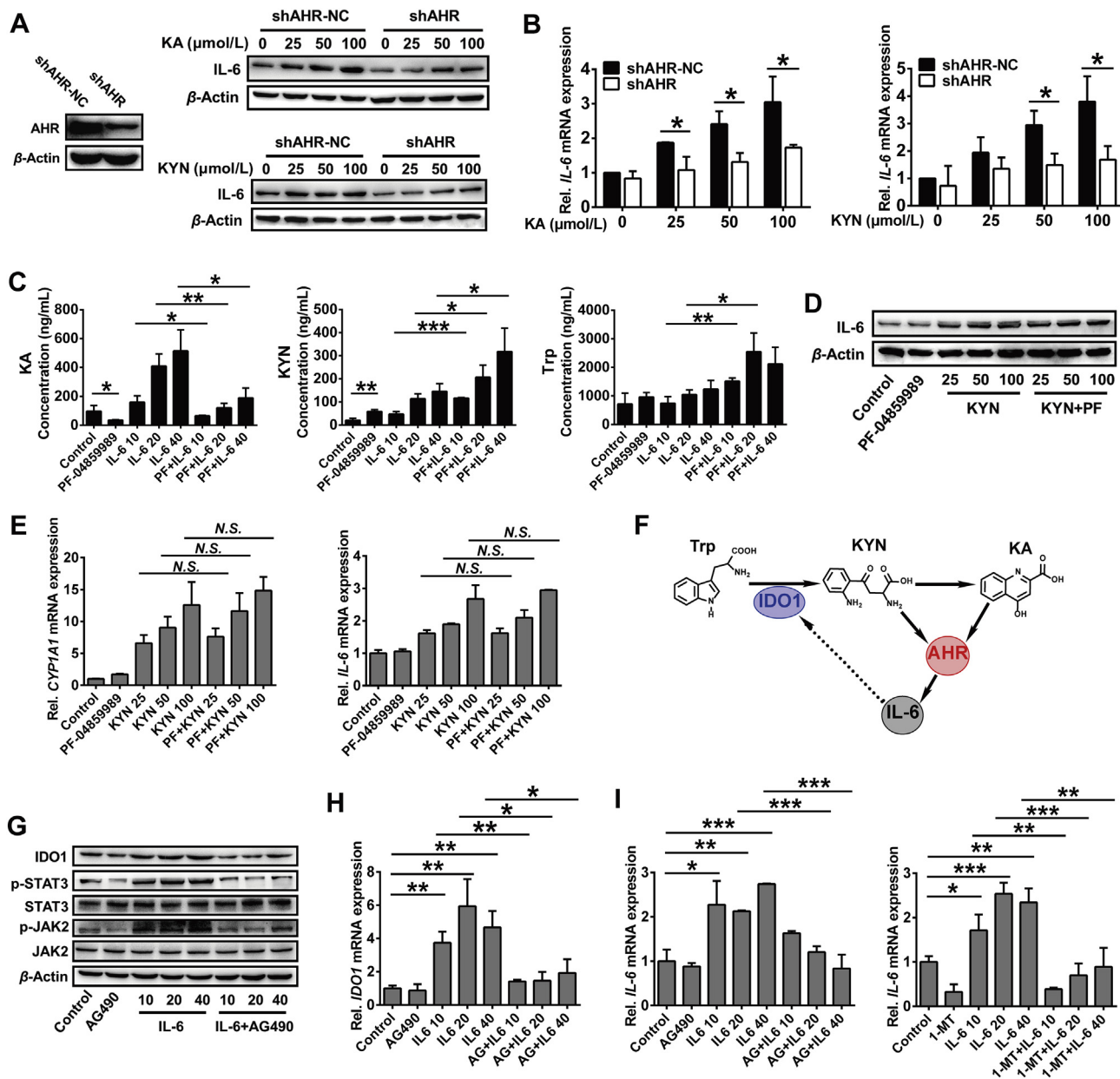


**Figure 2** IL-6-IDO1-AHR loop promotes the accumulation of KYN and KA through accelerating Trp-KYN-KA axis metabolism. Western blot and RT-PCR analysis of IL-6 protein (A) and mRNA (B) expression in *AHR* knockdown NCM460 cells that were treated with KYN and KA for 48 h ( $n = 3$ ). (C) LC-MS/MS quantitative analysis of the effect of KAT inhibitor PF-04859989 (PF, 5  $\mu\text{mol/L}$ ) on the metabolic changes of Trp, KYN and KA induced by IL-6 in NCM460 cells ( $n = 3$ ). (D) Western blot analysis of the effect of blocking KAT activity by PF on the expression of IL-6 induced by KYN in NCM460 cells. (E) RT-PCR analysis of CYP1A1 (*AHR* target gene) and IL-6 mRNA expression in NCM460 cells that were pretreated with (or without) PF-04859989 for 2 h prior to KYN treatment for 48 h ( $n = 3$ ). (F) The proposed schematic form of IL-6-IDO1-AHR positive feedback loop accelerates Trp-KYN-KA axis metabolism. (G) Western blot analysis of IDO1, phospho-STAT3 and phospho-JAK2 expression in NCM460 cells that were pretreated with (or without) JAK2/STAT3 pathway inhibitor AG490 (10  $\mu\text{mol/L}$ ) for 2 h prior to IL-6 treatment for 48 h. (H) RT-PCR analysis of *IDO1* mRNA expression in NCM460 cells that were pretreated with (or without) AG490 for 2 h prior to IL-6 treatment for 48 h ( $n = 3$ ). (I) RT-PCR analysis of the effect of blocking JAK2/STAT3 pathway by AG490 or KYN metabolic pathway by 1-MT on IL-6 mRNA expression in NCM460 cells stimulated by IL-6 itself ( $n = 3$ ). Data are presented as mean  $\pm$  SD. Statistical analysis was performed using Student's *t* test. \* $P < 0.05$ , \*\* $P < 0.01$  and \*\*\* $P < 0.001$ .

Primarily, we inhibited KAT activity using its specific inhibitor PF. As the results shown in Fig. 2C, cell KA level was sharply reduced and KYN level was significantly increased after PF treatment, indicating that the metabolism of KYN to KA was blocked. Then, we treated colonic epithelial cells with various concentrations of KYN. Clearly, we found that PF had no significant effect on AHR activity, IL-6 protein and mRNA

expression induced by KYN compared with KYN alone treatment group (Fig. 2D and E). These results indicate that AHR has a similar response sensitivity to KYN and KA.

According to the above results, we wonder whether there was a positive feedback regulation loop, describing as IL-6 promotes KYN pathway metabolism and AHR further promotes IL-6 expression through sensing KYN and KA levels, accelerating

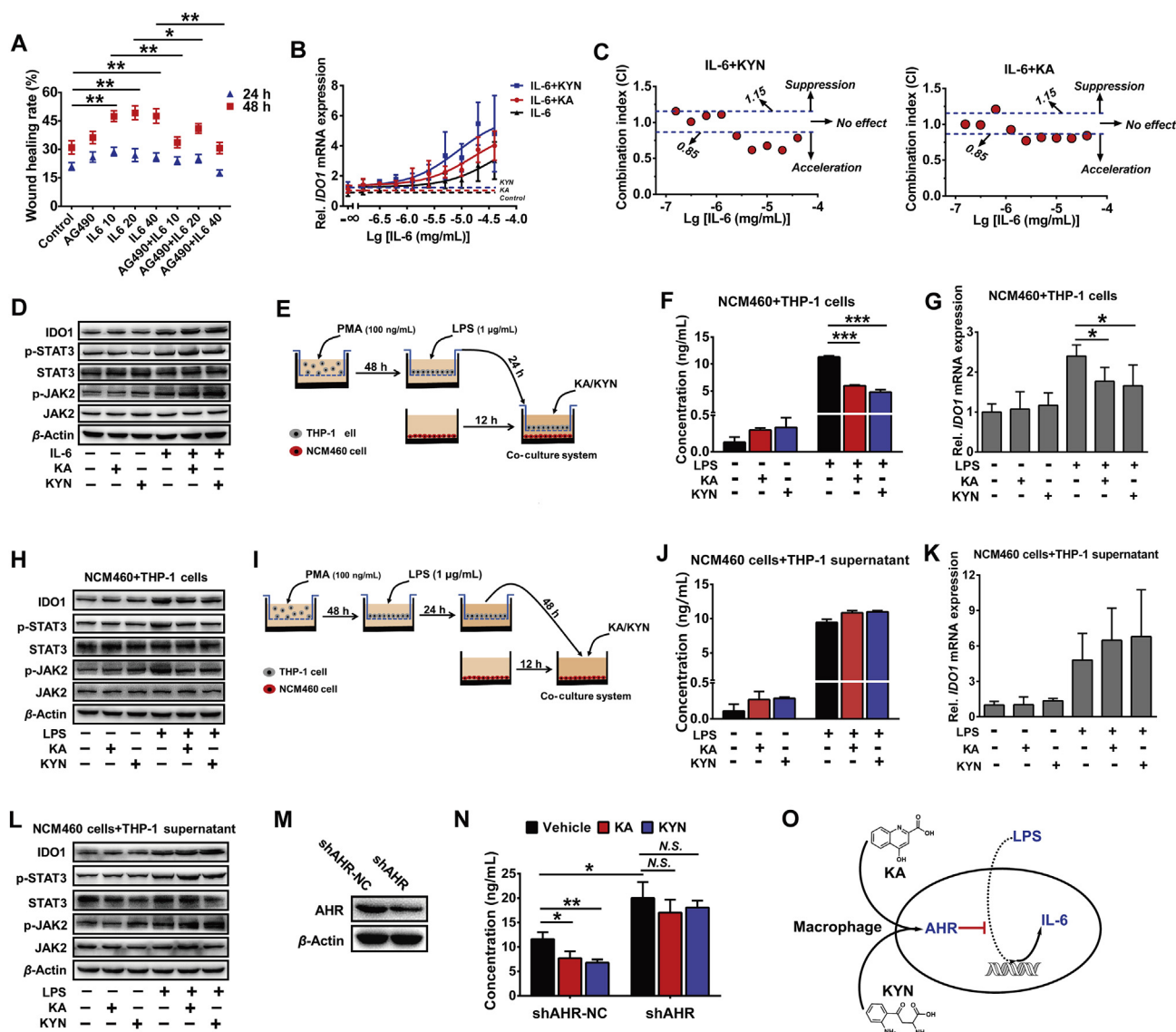


**Figure 3** Pathological inflammation plays a key role in triggering IL-6-IDO1-AHR loop formation. (A) Quantitative analysis of the effect of AG490 on NCM460 cell migration induced by IL-6 ( $n = 3$ ). (B) RT-PCR analysis of *IDO1* mRNA expression in NCM460 cells treated with IL-6 in combination with KYN or KA (25 μmol/L, respectively) for 48 h ( $n = 3$ ). (C) Combination index (CI) analysis was performed according to previous reports<sup>39,40</sup> to determine the synergistic effect of IL-6+KYN/KA on the expression of IDO1. CI values are interpreted as follows: <math>< 0.85</math> synergistic acceleration, >1.15 antagonistic suppression, 0.85–1.15 nearly additive. (D) Western blot analysis of IDO1, phospho-STAT3 and phospho-JAK2 expression in NCM460 cells treated with IL-6 (20 ng/mL) in combination with KYN or KA (25 μmol/L, respectively) for 48 h. Schematic construction of the co-culture intestinal inflammation model combining NCM460 with THP-1 cells (E, a) or its supernate (I, b). IL-6 levels in the supernate of a (F) and b (J) co-culture systems were detected using ELISA method after KA and KYN treatment ( $n = 3$ ). RT-PCR analysis of *IDO1* mRNA expression in the NCM460 cells of a (G) and b (K) co-culture system after KA and KYN treatment ( $n = 3$ ). Western blot analysis of IDO1 protein, phospho-STAT3 and phospho-JAK2 expression in the NCM460 cells of a (H) and b (L) co-culture system after KA and KYN treatment ( $n = 3$ ). (M) Western blot analysis of the expression of AHR in THP-1 cells after AHR gene knockdown using shRNA. (N) ELISA detection of IL-6 level in the supernate of AHR knockdown THP-1 cells that were induced by PMA, stimulated with LPS and KYN or KA for 48 h ( $n = 3$ ). (O) The proposed schematic form of KYN and KA suppressed LPS-induced IL-6 expression in macrophage through activating AHR. Data are presented as mean  $\pm$  SD. Statistical analysis was performed using Student's  $t$  test. \* $P < 0.05$ , \*\* $P < 0.01$  and \*\*\* $P < 0.001$ .

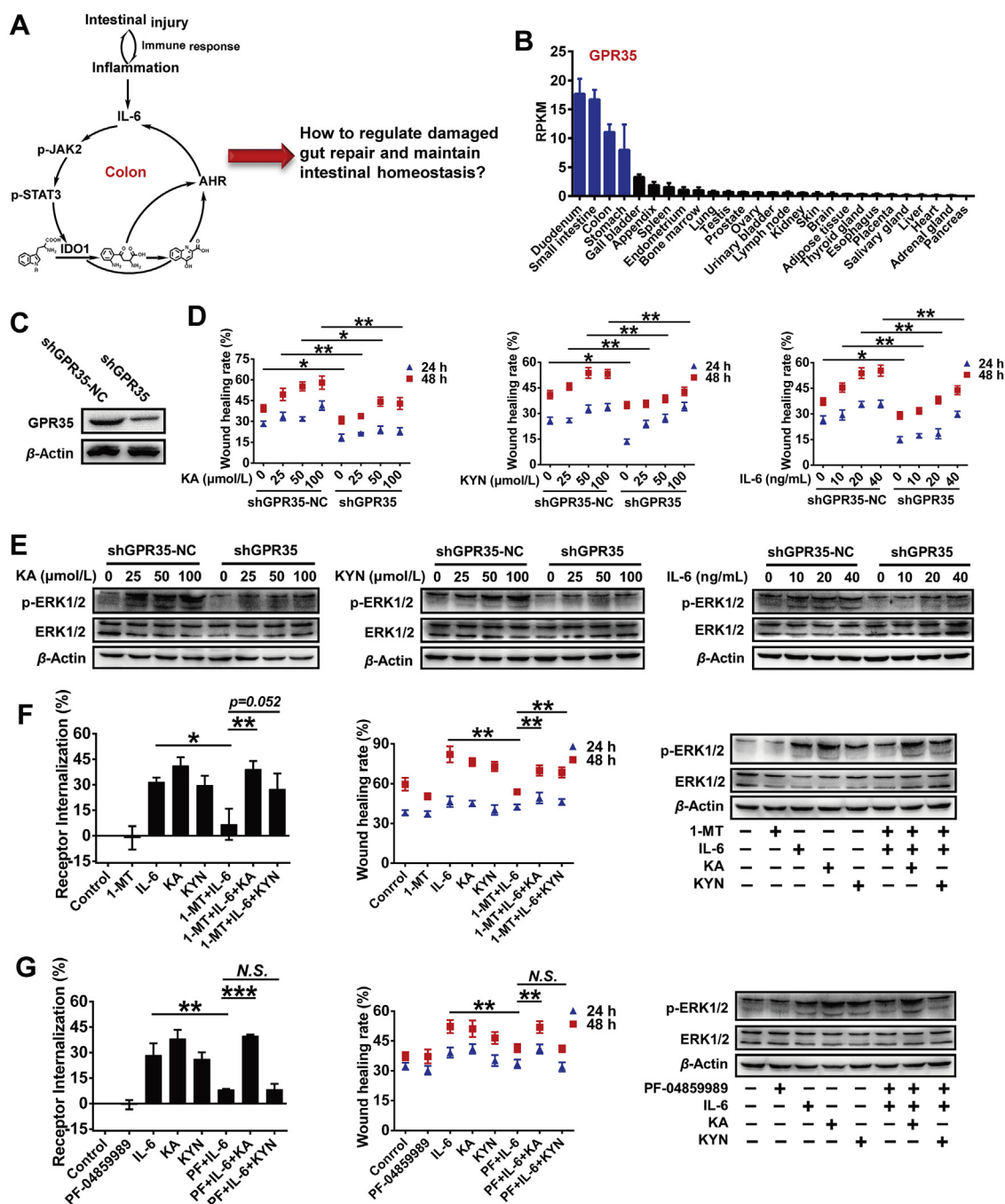


**Figure 4** GPR35 regulates colonic epithelial cell migration through sensing KA level. (A) The proposed schematic form of the mechanism that KYN and KA accumulated in damaged gut caused by chemotherapeutic toxicity. (B) The RPKM value (reads per kilobase per million mapped reads) of GPR35 gene in human multifarious tissues based on NCBI Gene Database analysis was used to determine the tissue-specificity of all protein-coding genes ( $n = 2-7$ ). (C) Western blot analysis of GPR35 protein expression in NCM460 cells after GPR35 gene knockdown. (D) Quantitative analysis of the effect of *GPR35* knockdown on KYN, KA and IL-6 induced monolayer NCM460 cell migration, showing wound healing rate as compared with initial scratch size ( $n = 3$ ). (E) Western blot analysis of the phosphorylation of ERK1/2 in GPR35 knockdown NCM460 cells after KYN, KA and IL-6 treatment for 48 h. Flow cytometry, wound healing and Western blot analyses of GPR35 receptor internalization (left panel), cell migration (middle panel) and phospho-ERK1/2 expression (right panel) respectively in NCM460 cells that were pretreated with (or without) PF-04859989 (PF, 5  $\mu\text{mol/L}$ ; F) or 1-MT (0.5  $\text{mmol/L}$ ; G) for 2 h prior to IL-6, or supplemented with KYN and KA treatment for 48 h ( $n = 3$ ). Data are presented as mean  $\pm$  SD. Statistical analysis was performed using Student's *t* test. \* $P < 0.05$ , \*\* $P < 0.01$  and \*\*\* $P < 0.001$ .

the accumulation of KYN and KA in gut (Fig. 2F). To confirm this hypothesis, we firstly explored the relationship between IL-6 and IDO1 expression. The Western blot and RT-PCR analysis demonstrate that IL-6 significantly promoted IDO1 protein and mRNA expression. Besides, we observed that IL-6 markedly promoted the phosphorylation of JAK2 and STAT3 expression in colonic epithelial cells (Fig. 2G and H). Meanwhile, we also found that there are multiple binding sites of STAT3 in the promoter regions of the human IDO1 gene (Supporting Information Fig. S4A). Thus, in order to further verify the role of the JAK2/STAT3 pathway played in IL-6-induced IDO1 expression, JAK2/STAT3 pathway specific inhibitor AG490 was utilized. We found that IL-6 induced IDO1 protein and mRNA expression were significantly inhibited by AG490 (Fig. 2G and H). Consistently, the metabolic level of Trp–KYN–KA axis induced by IL-6 in colonic epithelial cells was also significantly inhibited after AG490 treatment (Fig. S4B). More importantly, IL-6 treatment could significantly promote its own mRNA expression compared with vehicle control. This effect could also be markedly blocked when JAK2/STAT3 pathway or Trp–KYN–KA axis metabolism was inhibited (Fig. 2I). Collectively, our results suggest that KYN and KA serve as the core component of IL-6–IDO1–AHR positive feedback loop sensed by AHR.

#### 3.4. IL-6–IDO1–AHR loop was driven in a pathological inflammatory dependent mode

Positive feedback loop plays an important role in the cellular signaling amplification and rapid switching<sup>38</sup>. Thus, IL-6–IDO1–AHR regulation loop would accelerate the migration of intestinal epithelial cells. Indeed, the cells wound healing was significantly promoted during exogenous IL-6 administration, and the speed was obviously slowed down when IL-6–IDO1–AHR loop was blocked through interdicting JAK2/STAT3 pathway or Trp–KYN–KA axis metabolism (Figs. 1G and 3A; Figs. S2F and S4C). However, unexpectedly, the expression of IDO1 protein and mRNA, the phosphorylation of JAK2 and STAT3 could not be significantly induced by KYN or KA alone (Supporting Information Fig. S5A and S5B). These results suggest that the IL-6–IDO1–AHR positive feedback loop was not generated effectively. Cogitatively, we speculate that the autocrine IL-6 of intestinal cells induced by KYN or KA was not enough to drive the loop. Cytokines which produced by pathological inflammation might be a key trigger for the formation of the IL-6–IDO1–AHR loop.

To prove this hypothesis, we administered intestinal epithelial cells with KYN or KA at a concentration of 25  $\mu\text{mol/L}$  supplemented with gradient IL-6. Interestingly, the results reveal that KYN or KA further partly promoted *IDO1* mRNA expression under various concentrations of IL-6 stimuli compared with IL-6 alone treatment group (Fig. 3B). However, there wasn't a significant change ( $P > 0.05$ ). Circumspectly, we calculated the combination index to evaluate their synergistic effect according to the previous reports with a modification<sup>39,40</sup>. As the results demonstrate, there was an obvious synergistic effect of combining KYN or KA with IL-6 on IDO1 expression when the administrated IL-6 concentration exceeded 2.5 ng/mL (Fig. 3C). Subsequently, we examined the expression changes of loop's related proteins after combined application of KYN or KA with IL-6. The results demonstrate that the expression of IDO1 and the phosphorylation of JAK2 and STAT3 could be further promoted by KYN and KA under the IL-6 condition (Fig. 3D), indicating that under the IL-6 environment, the increase of KYN and KA level successfully

trigger the formation of IL-6–IDO1–AHR loop. Besides, we also found that consistent with that of IL-6, combining KYN or KA with IL-1 $\beta$  or TNF- $\alpha$  also exhibited a similar effect on the expression of IDO1 (except the combining of KYN with TNF- $\alpha$ ), although their effective concentration of synergy was difference (Fig. S5C and S5D). Collectively, these results confirm that inflammatory environment was necessary to trigger the formation of IL-6–IDO1–AHR positive feedback loop in gut.

#### 3.5. AHR negatively mediates LPS-induced IL-6 expression in macrophage

To better simulate the actual pathologic situation *in vivo* and reveal the relationship between Trp–KYN–KA axis metabolism and pathological inflammation, we constructed co-culture model of intestinal epithelial cells and macrophages. As Fig. 3E shows, we firstly co-cultured PMA and LPS-pretreated THP-1 and NCM460 cells, meanwhile, KYN or KA were administered. Unexpectedly, the results show that IL-6 production of co-culture system, IDO1 protein and mRNA expression and JAK2 and STAT3 phosphorylation of NCM460 cells were significantly inhibited after KYN and KA treatment (Fig. 3F–H). However, in the non-LPS-pretreated THP-1 and NCM460 cells co-culture system, the IL-6 level was partially elevated, and IDO1 protein and mRNA expression and the phosphorylation of JAK2 and STAT3 were not noticeably changed after the KYN and KA treatment (Fig. 3F–H). We speculate that this effect might be caused by AHR negatively regulate LPS-induced IL-6 expression in macrophages. Thus, we established another co-culture system, shown in Fig. 3I, where NCM460 cells were cultured with the supernatant of LPS-pretreated macrophage. Surprisingly, we found that the IL-6 level, IDO1 protein and mRNA expression and the phosphorylation of JAK2 and STAT3 in different modules had a rising trend after KYN and KA application (Fig. 3J–L). To further confirm the role of AHR in macrophages, we silenced *AHR* gene expression (Fig. 3M). Consistently, we observed that IL-6 expression induced by LPS was significantly inhibited by KYN or KA, and this effect was abolished after *AHR* knockdown (Fig. 3N). These results demonstrate that in contrast to intestinal epithelial cells, in macrophage KYN and KA inhibited LPS-induced IL-6 expression through activating AHR (Fig. 3O). What's more, IL-6 produced by macrophage could serve as the initiating impetus to drive the formation of the IL-6–IDO1–AHR loop, for its far more than that secreted by intestinal epithelial cells (Fig. 3F and J).

#### 3.6. GPR35 negative feedback regulates intestinal damage through sensing KA level selectively

By now, we have uncovered the role of KYN and KA in the intestinal epithelial cells migration and revealed the potential reason for their accumulation after drug-induced intestinal injury. However, the mechanism of gut tissue repair after damage was still unclear (Fig. 4A). To explore this, we primarily analyzed the gene expression of normal human tissues based on NCBI Gene Database. Fascinatingly, we found that GPR35 highly expressed in the human gastrointestinal tract<sup>41</sup> (Fig. 4B). GPR35 is a poorly characterized G protein-coupled receptor that has been shown to be activated by KA at micromolar concentrations which can be achieved in peripheral tissues under pathological condition<sup>25,42</sup>. To clarify whether GPR35 plays a key role in regulating damaged gut repair through sensing KYN pathway metabolism, we firstly performed knockdown of *GPR35* gene expression in intestinal epithelial cells (Fig. 4C). After treatment, we found that the

migration of NCM460 cells promoted by KYN, KA and IL-6 were markedly suppressed (Fig. 4D; Supporting Information Fig. S6A). More importantly, we observed that the phosphorylation of extracellular signal-regulated kinase 1/2 (ERK1/2), one of the downstream effector molecules of GPCR<sup>42,43</sup>, was significantly promoted after KA, KYN and IL-6 treatment. All these effects were markedly inhibited when the *GPR35* gene was silenced (Fig. 4E). Considering the promotion effect of IL-6 on the KYN metabolic pathway, we subsequently inhibited IDO1 activity and JAK2/STAT3 pathway respectively. Interestingly, we found that GPR35 internalization which is frequently used to characterize GPR35 response<sup>43</sup> was significantly increased after IL-6 administration. However, this effect was markedly blocked when cells were pretreated with 1-MT or AG490 (Fig. S6B). Moreover, the phosphorylation of ERK1/2 induced by IL-6 was also inhibited after KYN pathway metabolism is blocked (Fig. S6C). Scrupulously, we also used a specific GPR35 inhibitor (ML194) for further verification. Consistently, the results demonstrated that cell migration, GPR35 internalization and ERK1/2 phosphorylation induced by KYN and KA were significantly suppressed by ML194 (Fig. S6D–S6F). Collectively, these results demonstrate that GPR35 serves as the guardian of the kynurenine pathway metabolism and plays a key role in intestinal wound healing.

In order to further clarify the selectivity of GPR35 in response to KYN and KA, a program of irritant application was administered in intestinal epithelial cells. We primarily inhibited Trp catabolism to KYN pathway by 1-MT, followed by KYN or KA was supplemented after IL-6 treatment. The obvious inhibiting effect of 1-MT on IL-6 induced GPR35 response was found. Intestinal cells migration and ERK1/2 phosphorylation were also dramatically recovered after supplementing with KYN and KA separately in 1-MT + IL-6 group (Fig. 4F and Supporting Information Fig. S7A). Subsequently, we inhibited KYN metabolism using PF. Consistent with IDO1 inhibition, when KAT was suppressed, IL-6 induced GPR35 response, intestinal cells migration and ERK1/2 phosphorylation were all significantly inhibited (Fig. 4G and Fig. S7B). Interestingly, there was no obvious recovery when KYN was supplemented in PF + IL-6 group. However, it was quite different when KYN was replaced by KA (Fig. 4G and Fig. S7B). Finally, the effect of KYN and KA alone without the influence of IL-6 was also explored. We found that inhibiting KAT had no significant effect on KA induced GPR35 response, intestinal cell migration and ERK1/2 phosphorylation. Nevertheless, GPR35 response, cell migration and p-ERK1/2 expression induced by KYN were significantly repressed when KAT activity was blocked. Additionally, these effects could be dramatically reverted after supplementing with KA in PF + KYN group (Fig. S7C–S7E). All the above results reveal that GPR35 promotes the repair of damaged gut through sensing KA selectively.

### 3.7. AHR and GPR35 sense KA in a gradient mode to feedback regulate intestinal damage

Metabolic adaptations could defend cellular, tissue, and systemic homeostasis through specific sensors by monitoring the change of endogenous metabolites<sup>44,45</sup>. Here, our study demonstrates the dramatic accumulation of KYN and KA in damaged gut, which stress AHR/GPR35 systems response. Thus, to further uncover the metabolic regulation of KYN pathway in chemotherapeutics-induced intestinal damage, we explored the sensitivity difference of AHR and GPR35 in response to KA level. As the results

demonstrate that the EC<sub>50</sub> of GPR35 response to KA was 46.16  $\mu\text{mol/L}$  far exceeding the value of 11.44  $\mu\text{mol/L}$  of AHR response (Fig. 5A and B), suggesting the characteristic of gradient sensing of AHR and GPR35 to KA level in gut (Fig. 5C). Collectively, the mechanism of AHR and GPR35 feedback regulate intestinal injury to maintain intestinal homeostasis through gradiently sensing KA level was depicted (Fig. 5D). At the initiation of drug-induced intestinal damage, macrophage infiltrated into injured tissues and produced abundant IL-6, which accelerated KYN pathway metabolism through promoting IDO1 expression *via* JAK2/STAT3 pathway. The increase of KYN and KA were primarily sensed by AHR. Activated AHR promoted IL-6 autocrine in intestinal cells, which triggered the formation of the IL-6–IDO1–AHR positive feedback loop and further accelerated the KYN pathway metabolism. Subsequently, GPR35 negative feedback regulated intestinal damage through specifically sensing KA level. It is worth noting that AHR negatively regulated LPS-induced IL-6 expression in macrophage (Fig. 3O), in contrast with colon cells. These results constitute a rationale of defense responses against intestinal damage.

### 3.8. Discovering AHR and GPR35 agonists from approved drugs

Our above researches suggest that pharmacological activation of AHR and GPR35 during chemotherapy might be a promising intervention strategy to restrict the occurrence and development of intestinal damage. However, currently, there is no approved drug target at GPR35 or AHR. To further explore the clinically effective interventions, we screened 2388 approved drugs from Drug-Bank Database using virtual screening method to find out AHR and GPR35 agonists. As shown in Fig. 5E, we primarily constructed the homology modeling of GPR35 and AHR proteins, since there were a lack of the practicable proteins crystal structure in RCSB Protein Data Bank database. The modeling results of GPR35 and AHR are exhibited in Supporting Information Fig. S8A and S8B, and the Ramachandran plots of GPR35 and AHR show that more than 98% residues were in the allowed regions, indicating that the 3D structures of the models were reasonable. Subsequently, molecular docking was performed respectively and the docking scores were used as indicator to evaluate the possibility of drug being an agonist for each target. We selected the top 50 hits to perform further screening based on pharmacokinetics, toxicology and other clinical data (Supporting Information Tables S8 and S9). Eventually, 10 potential GPR35 and 11 potential AHR agonists were acquired (Fig. S8C). Among them, vardenafil (Vard), known as a PDE5 inhibitor for the treatment of erectile dysfunction, exhibited the greatest promotion of GPR35 internalization and ERK1/2 phosphorylation in intestinal epithelial cells (Fig. S8D–S8F). Besides, linagliptin (Linag), known as a DPP-4 inhibitor for the treatment of type II diabetes, exhibited the greatest promotion to the expression of CYP1A1 protein and mRNA in macrophage (Fig. S8G and S8H). These results suggest that Vard and Linag were the agonists of GPR35 and AHR, respectively. Moreover, Linag could partly promote GPR35 internalization and ERK1/2 phosphorylation, which indicates that Linag was also a GPR35 agonist although weaker than Vard (Fig. S8E and S8F). Further study revealed that, Vard and Linag had no significant effect on the expression of GPR35 and AHR proteins, respectively (Fig. S8F and S8H), which suggest that they were directly binding to GPR35 and AHR, rather than altering their expression, leading to the downstream signal transduction.

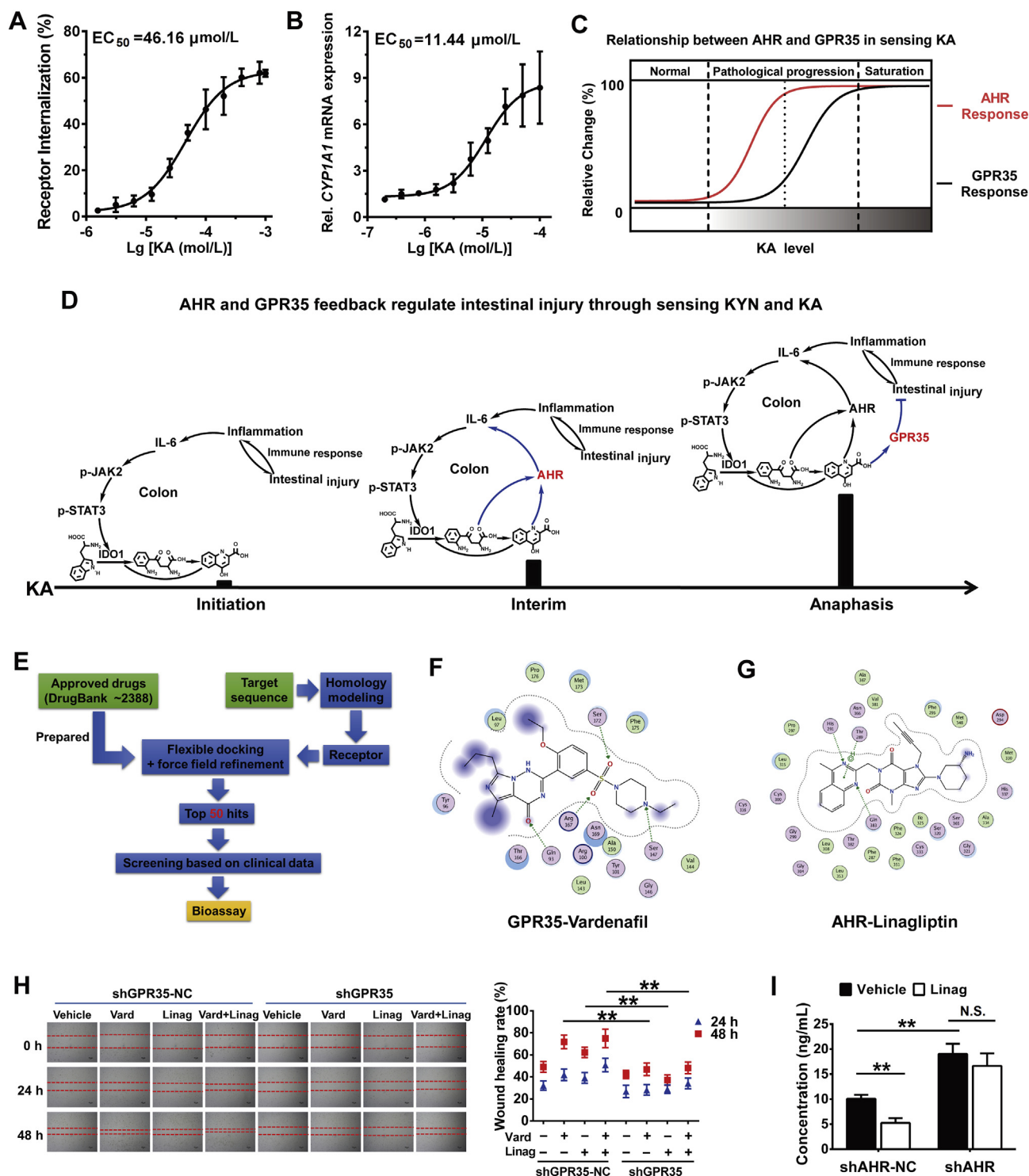


**Figure 5** Trp–KYN–KA axis metabolism sensing drives the discovery of drug intervention. (A) Concentration response curve of GPR35 receptor internalization to determine GPR35 activity detected by flow cytometry after NCM460 cells treated with KA for 48 h ( $n = 3$ ). (B) Concentration response curve of *CYP1A1* mRNA expression to determine AHR activity detected by RT-PCR after NCM460 cells treated with KA for 48 h ( $n = 3$ ). Data are presented as means  $\pm$  SD, the EC<sub>50</sub> value was calculated by graphpad prism software. (C) The illustration of gradient sensing relationship between AHR and GPR35 in pathological progression. Gray shading signifies KA level in intestinal tissue. (D) Schematic of how the gut drives defensive response against drug-induced intestinal damage by coordinating AHR and GPR35-mediated metabolic sensing. (E) The flowchart of structure-based virtual screening. The binding modes of vardenafil (Vard)–GPR35 (F) and linagliptin (Linag)–AHR (G). Green dotted line signifies hydrogen bond. (H) Wound healing and quantification analyses of the migration of GPR35 knockdown NCM460 cells after treated with Vard, Linag and their combination for 24 and 48 h (mean  $\pm$  SD,  $**P < 0.01$ ; Student's *t* test,  $n = 3$ ). (I) ELISA detection of IL-6 level in the supernate of AHR knockdown THP-1 cells that were differentiated by PMA, stimulated with LPS and Linag for 48 h (mean  $\pm$  SD,  $**P < 0.01$ ; Student's *t* test,  $n = 3$ ).

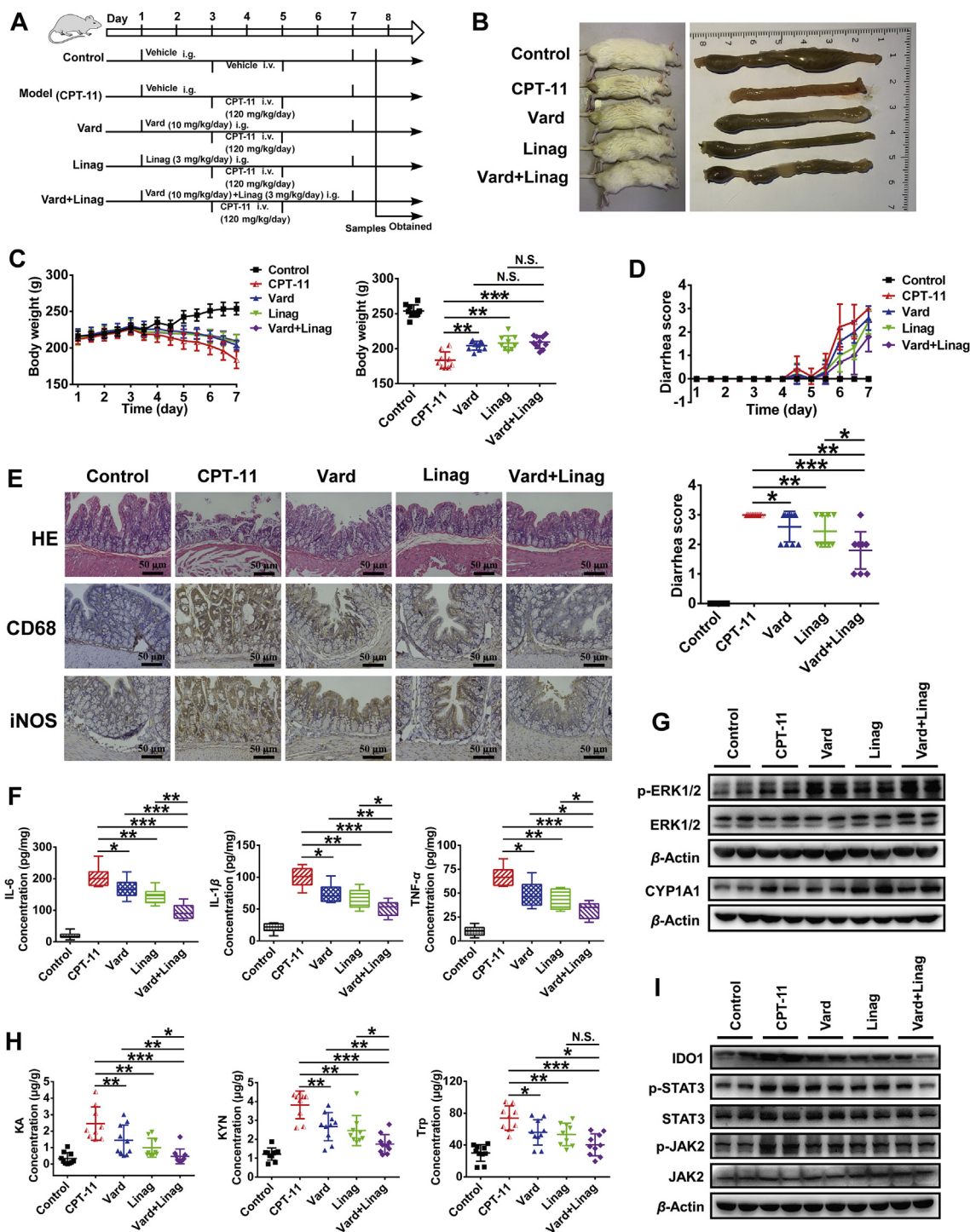


**Figure 6** Vard and Linag attenuate irinotecan-induced rat intestinal toxicity. (A) Schematic of Vard, Linag and their combination intervene CPT-11 induced rat intestinal toxicity. (B) Representative images of rats and their corresponding colon tissues after drug administration. The body weight (C) and diarrhea score (D) of each rat were monitored twice daily showing as mean  $\pm$  SD, and the values of the seventh day were shown independently. (E) HE staining and immunohistochemistry analyses of CD68 and iNOS were performed on rat colon after drug administration. (F) ELISA detection of IL-6, IL-1 $\beta$  and TNF- $\alpha$  levels in rat colon after drug administration. (G) Western blot analysis of phospho-ERK1/2 and CYP1A1 proteins expression in rat colon after drug administration. (H) LC-MS/MS quantitative analysis the levels of Trp, KYN and KA in rat colon after drug administration. (I) Western blot analysis of IDO1, phospho-JAK2 and phospho-STAT3 proteins expression in rat colon after drug administration. Data are presented as mean  $\pm$  SD. Statistical analysis was performed using Student's *t* test. \**P* < 0.05, \*\**P* < 0.01 and \*\*\**P* < 0.001.

For the binding model of GPR35 and Vard, the oxygen atoms of sulfony and keto groups form three hydrogen bond with the side-chain residues of Ser172, Arg167 and Gln93, respectively, and the nitrogen atom of piperazine group forms one hydrogen bond with the side-chain residue of Ser147 (Fig. 5F). For the binding model of AHR and Linag, the nitrogen atoms of quinoxaline group form two hydrogen bond with the side-chain residues of His291 and Gln383, respectively, and the pyrimidine ring of quinoxaline group forms a  $\pi$ -H conjugate with the side-chain residue of Thr289 (Fig. 5G). Besides, for the binding model of GPR35 and Linag, the oxygen atom of purine group forms one hydrogen bond with the side-chain residue of Arg167, and the carton atom forms one hydrogen bond with the backbone of residue Ala 150 (Fig. S8I).

Next, we verified whether GPR35 and AHR played key roles in Vard- and Linag-regulated pharmacological activities *in vitro*. The results show that Vard and Linag could significantly promote wound healing of intestinal epithelial cells, and the effect would be markedly inhibited once GPR35 was silenced (Fig. 5H). Meanwhile, Linag obviously inhibited the expression of IL-6 in macrophage, and the effect was also obviously blocked after AHR was silenced (Fig. 5I). The above results demonstrate that Vard and Linag would be the promising intervention agents in alleviating chemotherapy-induced intestinal toxicity through activating GPR35 and AHR.

### 3.9. Vard and Linag attenuate chemotherapy-induced intestinal toxicity *in vivo*

To further investigated the effect of Vard and Linag on intervening chemotherapy-induced intestinal toxicity *in vivo*, we constructed CPT-11-induced rat diarrhea model, and the rat administrative program is shown in Fig. 6A. Attractively, it is clearly observed that the model group rats became languid and extremely emaciated, with the feces as watery stool and the colon tissue inflamed and accompanied with hemorrhage after CPT-11 treatment. However, these symptoms were dramatically alleviated after Vard and Linag administration (Fig. 6B). Through daily record, we found that Vard and Linag could significantly suppress CPT-11-induced rat body weight reduction and diarrhea score augmentation (Fig. 6C and D). Moreover, combining Vard with Linag exhibited a further and remarkable attenuation to CPT-11-induced rat diarrhea compared with the application of either alone, although the body weight had no significant difference between them (Fig. 6C and D). Furthermore, histopathological examination demonstrates that Vard and Linag observably improved CPT-11 caused severe colon damage and macrophage infiltration. Besides, it is heartening that combining Vard with Linag revealed a more powerful effect on alleviating CPT-11-induced intestinal toxicity (Fig. 6E). Moreover, the proinflammatory cytokines IL-6, IL-1 $\beta$  and TNF- $\alpha$  consistently displayed a similar variation profile in colon and serum (Fig. 6F and Supporting Information Fig. S9). Collectively, these data reveal that combining Vard with Linag is a promising intervention strategy in attenuating chemotherapy-induced intestinal toxicity.

Further assays were conducted to clarify whether Vard and Linag exert their effectiveness through binding with GPR35 and AHR, respectively. We firstly detected the expression of GPR35 and AHR targeted proteins in rat colon after treatment. The

results demonstrate that ERK1/2 phosphorylation and CYP1A1 expression in Vard and Linag groups were significantly promoted compared with control group (Fig. 6G). However, there was still a lack of evidence for a conclusion. Hence, we subsequently detected the metabolic level of the Trp-KYN-KA axis. It was clearly found that accompanying with the accumulation of KYN and KA, the ERK1/2 phosphorylation and CYP1A1 expression were also obviously promoted in the model group (Fig. 6G and H). Importantly, even though the levels of KYN and KA were significantly reduced in the drug intervention groups, conversely, ERK1/2 phosphorylation in Vard and Linag groups and CYP1A1 expression in Linag group were significantly elevated compared with the model group (Fig. 6G and H). Current evidence reveals that Vard and Linag alleviated CPT-11-induced intestinal toxicity through activating GPR35 and AHR separately.

Furthermore, as Fig. 5D demonstrates, we also observed that IDO1 and IL-6 expression, JAK2 and STAT3 phosphorylation and AHR activity were significantly promoted after CPT-11 caused intestinal damage, which suggests that the positive feedback loop was triggered in colon (Fig. 6F-I). Attractively, after Vard and Linag intervention, accompanied with the relief of symptoms, all signals of the loop, except AHR for the continuous activation by Linag, were dramatically weakened. Especially, the combination of Vard and Linag exhibited a further weakening to the loop's signals compared with their administration alone (Fig. 6F-I). Therefore, the IL-6-IDO1-AHR loop was basically blocked for the recovery of intestinal homeostasis. Together, this work provides a promising intervention strategy for attenuating chemotherapy-induced intestinal toxicity.

## 4. Discussion

Cellular and tissue homeostasis is a key physiological variable and is maintained by the interaction of metabolites and their monitor<sup>22,26</sup>. Understanding these systems is imperative to minimize health problems and has important implications for many pathological conditions, including chemotherapeutics-induced intestinal damage. Intestinal toxicity caused by anti-cancer medicines has become a nonnegligible clinical problem. Consistently, our study exhibited that the intestinal homeostasis was severely destroyed after rat was exposed to anticarcinogens. The rats manifested serious gut injury, metabolic disorders and accompanied with inflammatory response for macrophages infiltration and inflammatory cytokines release. Interestingly, we also found that diverse chemotherapeutics-induced intestinal damage was commonly characterized by the sharp upregulation of Trp-KYN-KA axis metabolism. Under pathophysiologic conditions, KYN and KA were accumulated in peripheral tissues in the nmol/L to  $\mu$ mol/L range. However, their biological effects and underlying mechanisms remain mysterious<sup>25,46</sup>. In this work, our data demonstrate that inflammatory cytokines especially IL-6 could promote IDO1 expression through JAK2/ATAT3 pathway. This process plays a key role in the accumulation of KYN and KA in colon. Meanwhile, the accumulated KYN and KA might further promote IL-6 autocrine in enterocyte through AHR sensing. As a result, the transition of Trp to KYN was further amplified by the IL-6-IDO1-AHR positive feedback loop. Interestingly, pathological inflammatory environment is indispensable to the formation of IL-6-IDO1-AHR loop, which is

not exist in the normal intestinal tissues. Under the pathological state, damaged gut rapidly accumulates KYN and KA, which would serve as endogenous ligands to trigger a series metabolic response.

AHR and GPR35 are the downstream metabolic guardians of the KYN pathway. In this study, we proved that they constitute a feedback regulation system in gut to defend against chemotherapy-induced intestinal toxicity. GPR35 is an orphan receptor and is highly expressed in the gastrointestinal tract. GPR35 has been reported to be closely related to multiple diseases such as IBD, type II diabetes, and coronary artery disease<sup>47</sup>, whereas physiological stimuli regulate GPR35 remains enigmatic<sup>48</sup>. In this study, we observed that changing the metabolic synthesis of KA significantly influenced the GPR35 response and signal transduction. Besides, either silencing *GPR35* gene expression or inhibiting its activity can markedly suppress epithelial cells migration which is an essential physiological process for intestinal repair and homeostasis<sup>49,50</sup>. All these findings demonstrate that GPR35 negatively feedback regulated intestinal damage to promote colon repair and maintain intestinal homeostasis through sensing KA level selectively. We further identified that ERK1/2 phosphorylation was the downstream cascade signal of GPR35. AHR is a member of the PerArnt-Sim (PAS) superfamily of transcription factors and could regulate the expression of cytochrome P450s, most notably CYP1A1<sup>51,52</sup>. AHR could serve as the sensor of KYN and KA in both intestinal cells and macrophages. KYN and KA negatively regulate LPS-induced IL-6 expression in macrophages, contrary to the situation in intestinal epithelial cells. In macrophages, AHR forms a complex with STAT1 and nuclear factor-kappa B (NF- $\kappa$ B) under the stimulation of LPS. This suppresses the activation of IL-6 promoter<sup>53</sup>. However, in peripheral tissues, ligand-activated AHR may directly participated in priming IL-6 promoter through binding to non-consensus dioxin response elements that located upstream of the IL-6 start site<sup>54,55</sup>.

Meanwhile, our study also proved that AHR and GPR35 negative feedback regulation of intestinal damage and inflammation through gradually sensing kynurenic acid level. AHR exhibited a higher sensitivity in responding to KA level than GPR35. Thus, we divided the metabolic sensing of Trp–KYN–KA axis into three stages to elucidate the pathological progression of chemotherapy-induced intestinal damage. As demonstrated in Fig. 5D, chemotherapy-induced intestinal toxicity triggered the formation of IL-6–IDO1–AHR positive feedback loop through inflammation response. As a consequence, the accumulation of KYN and KA was accelerated, and sensed by GPR35. Then, AHR-mediated IL-6 inhibition in macrophage and autocrine in gut, GPR35-mediated intestinal wound repair form a temporary balance under the pathological condition. This balance would easily be destroyed by the persisted stimulation of chemotherapeutics and the following damaged phenotype would occur. Once drug is terminated, the immune response would suffer incessant weakening for the feedback regulation of GPR35 and AHR. After a period of delay, the responses of GPR35 and AHR to KYN pathway metabolism were diminished gradually until the gut reached the normal homeostasis (Supporting Information Fig. S10).

Our studies indicated that pharmacological manipulation of GPR35 and AHR might be a powerful approach to attenuate chemotherapy-induced intestinal toxicity. Unfortunately, up to now no drug targeting GPR35 and AHR proteins has been approved. Drug repurposing is becoming an increasingly attractive

strategy for drug discovery. It can bypass the common challenges associated with drug development and is more time- and cost-efficient<sup>56</sup>. Noteworthy, co-culture results demonstrated that although activating AHR in intestinal cells could promote IL-6 autocrine, the increase was far less than that produced by macrophages in which AHR plays a suppressive role in LPS-induced IL-6 expression (Fig. 3J). Furthermore, subjoining the AHR excitatory ligand in macrophage and enterocyte co-culture system significantly reduced the production of IL-6. Thus, as a whole, concurrently activating AHR and GPR35 would be more conducive to repair the damaged gut. In this work, a panel of 2388 approved drugs were screened by virtual and bioactivity screening approaches to discover the agonists of GPR35 and AHR protein. Fortunately, Vard and Linag were screened out. Vard, a PDE5 inhibitor for the treatment of erectile dysfunction, was screened out as GPR35 agonist. Linag, a DPP-4 inhibitor for the treatment of type II diabetes, was discovered as an agonist of both AHR and GPR35. Animal experiments verified that Vard and Linag alone or in combination could significantly attenuate chemotherapy-induced intestinal toxicity *via* binding with AHR and GPR35. What is more interesting is that combining Vard with Linag exhibited a more powerful effect compared with their single application.

## 5. Conclusions

Our results reveal a passive defense mechanism that AHR and GPR35 feedback regulate chemotherapy-induced intestinal damage to maintain intestinal integrity and homeostasis through sensing KA level in a gradient-dependent manner. The activating of GPR35 and AHR alone or together would lead to the attenuation of chemotherapy-induced intestinal toxicity. Vard and Linag were proved as GPR35 and AHR agonists, respectively, and they have a great potential in clinical application. Our study highlights the urgency and necessity of dual-targeting new drug development for the purpose of toxicity-reducing and efficacy-enhancing.

## Acknowledgments

The authors thank Doudou Xu, Xien Zhang, and Bei Tan from China Pharmaceutical University (Nanjing, China) for the help of animal drug administration and tissue samples collection. The authors also thank Dr. Zhihong Liu from Sun Yat-sen University (Guangzhou, China) for providing fore-mentioned modeling software and Wecomput Technology Co., Ltd. (Beijing, China) for providing computation consulting. This work was supported by the National Nature Science Foundation of China (NSFC Nos. 81773861 and 81773682), National Science and Technology Major Project (2017ZX09101001, China), Jiangsu Provincial National Science Foundation for Distinguished Young Scholars (No. BK20180027, China), Double First-Class University Project, the Program for Jiangsu province Innovative Research Team and a project funded by the Priority Academic Program Development of Jiangsu Higher Education Institutions (PAPD, China).

## Author contributions

Di Wang designed and performed experiments, analyzed and interpreted data, and wrote the manuscript. Danting Li constructed VCR-induced rat ileus model. Yuxin Zhang commented and proofread the manuscript. Jie Chen, Ying Zhang, Chuyao Liao,

and Siyuan Qin collected tissue samples and commented the manuscript. Yuan Tian guided instrument operation and maintenance. Fengguo Xu, Zunjian Zhang designed the experiments, commented the manuscript, administrative support and study supervision.

### Conflicts of interest

The authors declare that there are no conflicts of interest regarding the publication of this article.

### Appendix A. Supporting information

Supporting data to this article can be found online at <https://doi.org/10.1016/j.apsb.2020.07.017>.

### References

- Rubenstein EB, Peterson DE, Schubert M, Keefe D, McGuire D, Epstein J, et al. Clinical practice guidelines for the prevention and treatment of cancer therapy-induced oral and gastrointestinal mucositis. *Cancer* 2004;**100**:2026–46.
- Mitchell EP. Gastrointestinal toxicity of chemotherapeutic agents. *Semin Oncol* 2006;**19**:566–79.
- Dore MP, Pes GM, Murino A, Quarta Colosso B, Pennazio M. Short article: small intestinal mucosal injury in patients taking chemotherapeutic agents for solid cancers. *Eur J Gastroenterol Hepatol* 2017;**29**:568–71.
- Grattagliano I, Ubaldi E, Portincasa P. Drug-induced enterocolitis: prevention and management in primary care. *J Dig Dis* 2018;**19**:127–35.
- Rodrigues D, Souza T, Jennen DG, Lemmens L, Kleinjans JC, de Kok TM. Drug-induced gene expression profile changes in relation to intestinal toxicity: state-of-the-art and new approaches. *Canc Treat Rev* 2019;**77**:57–66.
- Gurwitz JH, Field TS, Harrold LR, Rothschild J, Debellis K, Seger AC, et al. Incidence and preventability of adverse drug events among older persons in the ambulatory setting. *J Am Med Assoc* 2003;**289**:1107–16.
- Prisciandaro LD, Geier MS, Butler RN, Cummins AG, Howarth GS. Evidence supporting the use of probiotics for the prevention and treatment of chemotherapy-induced intestinal mucositis. *Crit Rev Food Sci Nutr* 2011;**51**:239–47.
- Wardill HR, Bowen JM, Gibson RJ. New pharmacotherapy options for chemotherapy-induced alimentary mucositis. *Expert Opin Biol Ther* 2014;**14**:347–54.
- Sullivan LB, Gui DY, Vander Heiden MG. Altered metabolite levels in cancer: implications for tumour biology and cancer therapy. *Nat Rev Canc* 2016;**16**:680–93.
- Wishart DS. Emerging applications of metabolomics in drug discovery and precision medicine. *Nat Rev Drug Discov* 2016;**15**:473–84.
- Yao Y, Zhang P, Wang J, Chen J, Wang Y, Huang Y, et al. Dissecting target toxic tissue and tissue specific responses of irinotecan in rats using metabolomics approach. *Front Pharmacol* 2017;**8**:122.
- Cui DN, Wang X, Chen JQ, Lv B, Zhang P, Zhang W, et al. Quantitative evaluation of the compatibility effects of huangqin decoction on the treatment of irinotecan-induced gastrointestinal toxicity using untargeted metabolomics. *Front Pharmacol* 2017;**8**:211.
- Guo H, Jiao Y, Wang X, Lu T, Zhang Z, Xu F. Twins labeling-liquid chromatography/mass spectrometry based metabolomics for absolute quantification of tryptophan and its key metabolites. *J Chromatogr A* 2017;**1504**:83–90.
- Kaluzna-Czaplinska J, Gatarek P, Chirumbolo S, Chartrand MS, Bjorklund G. How important is tryptophan in human health?. *Crit Rev Food Sci Nutr* 2019;**59**:72–88.
- Cervenka I, Agudelo LZ, Ruas JL. Kynurenines: tryptophan's metabolites in exercise, inflammation, and mental health. *Science* 2017;**357**:eaaf9794.
- Platten M, Nollen EAA, Rohrig UF, Fallarino F, Opitz CA. Tryptophan metabolism as a common therapeutic target in cancer, neurodegeneration and beyond. *Nat Rev Drug Discov* 2019;**18**:379–401.
- Jia Xin Yu, Vanessa M, Hubbard-Lucey, Tang J. Immuno-oncology drug development goes global. *Nat Rev Drug Discov* 2019;**18**:899–900.
- Rohrig UF, Majjigapu SR, Vogel P, Zoete V, Michielin O. Challenges in the discovery of indoleamine 2,3-dioxygenase 1 (IDO1) inhibitors. *J Med Chem* 2015;**58**:9421–37.
- Dounay AB, Tuttle JB, Verhoest PR. Challenges and opportunities in the discovery of new therapeutics targeting the kynurenine pathway. *J Med Chem* 2015;**58**:8762–82.
- Lamas B, Natividad JM, Sokol H. Aryl hydrocarbon receptor and intestinal immunity. *Mucosal Immunol* 2018;**11**:1024–38.
- Metidji A, Omenetti S, Crotta S, Li Y, Nye E, Ross E, et al. The environmental sensor AHR protects from inflammatory damage by maintaining intestinal stem cell homeostasis and barrier integrity. *Immunity* 2018;**49**:353–62.
- Rothhammer V, Quintana FJ. The aryl hydrocarbon receptor: an environmental sensor integrating immune responses in health and disease. *Nat Rev Immunol* 2019;**19**:184–97.
- Agus A, Planchais J, Sokol H. Gut microbiota regulation of tryptophan metabolism in health and disease. *Cell Host Microbe* 2018;**23**:716–24.
- Husted AS, Trauelsen M, Rudenko O, Hjorth SA, Schwartz TW. GPCR-mediated signaling of metabolites. *Cell Metabol* 2017;**25**:777–96.
- Agudelo LZ, Ferreira DMS, Cervenka I, Bryzgalova G, Dadvar S, Jannig PR, et al. Kynurenic acid and Gpr35 regulate adipose tissue energy homeostasis and inflammation. *Cell Metabol* 2018;**27**:378–92.
- Tan JK, McKenzie C, Marino E, Macia L, Mackay CR. Metabolite-sensing G protein-coupled receptors-facilitators of diet-related immune regulation. *Annu Rev Immunol* 2017;**35**:371–402.
- Coumilleau P, Poellinger L, Gustafsson JA, Whitelaw ML. Definition of a minimal domain of the dioxin receptor that is associated with HSP90 and maintains wild type ligand binding affinity and specificity. *J Biol Chem* 1995;**270**:25291–300.
- MacKenzie AE, Caltabiano G, Kent TC, Jenkins L, McCallum JE, Hudson BD, et al. The antiallergic mast cell stabilizers lodoxamide and bufrolin as the first high and equipotent agonists of human and rat GPR35. *Mol Pharmacol* 2014;**85**:91–104.
- Lipinski CA. Lead- and drug-like compounds: the rule-of-five revolution. *Drug Discov Today Technol* 2004;**1**:337–41.
- Guo HM, Chen JQ, Huang Y, Zhang W, Xu FG, Zhang ZJ. A pseudo-kinetics approach for time-series metabolomics investigations: more reliable and sensitive biomarkers revealed in vincristine-induced paralytic ileus rats. *RSC Adv* 2016;**6**:54471–8.
- Reynell PC, Spray GH. The simultaneous measurement of absorption and transit in the gastro-intestinal tract of the rat. *J Physiol* 1956;**131**:452–62.
- Wang X, Cui DN, Dai XM, Wang J, Zhang W, Zhang ZJ, et al. HuangQin decoction attenuates CPT-11-induced gastrointestinal toxicity by regulating bile acids metabolism homeostasis. *Front Pharmacol* 2017;**8**:156.
- Kurita A, Kado S, Kaneda N, Onoue M, Hashimoto S, Yokokura T. Modified irinotecan hydrochloride (CPT-11) administration schedule improves induction of delayed-onset diarrhea in rats. *Cancer Chemother Pharmacol* 2000;**46**:211–20.
- Cooper HS, Murthy SN, Shah RS, Sedergran DJ. Clinicopathologic study of dextran sulfate sodium experimental murine colitis. *Lab Invest* 1993;**69**:238–49.

35. Jin BR, Chung KS, Cheon SY, Lee M, Hwang S, Noh Hwang S, et al. Rosmarinic acid suppresses colonic inflammation in dextran sulphate sodium (DSS)-induced mice *via* dual inhibition of NF- $\kappa$ B and STAT3 activation. *Sci Rep* 2017;**7**:46252.
36. Taleb S. Tryptophan dietary impacts gut barrier and metabolic diseases. *Front Immunol* 2019;**10**:2113.
37. Beischlag TV, Luis Morales J, Hollingshead BD, Perdew GH. The aryl hydrocarbon receptor complex and the control of gene expression. *Crit Rev Eukaryot Gene Expr* 2008;**18**:207–50.
38. Nishi A, Bibb JA, Snyder GL, Higashi H, Nairn AC, Greengard P. Amplification of dopaminergic signaling by a positive feedback loop. *Proc Natl Acad Sci U S A* 2000;**97**:12840–5.
39. Damon LE, Cadman EC. Advances in rational combination chemotherapy. *Canc Invest* 1986;**4**:421–44.
40. Kern DH, Morgan CR, Hildebrand-Zanki SU. *In vitro* pharmacodynamics of 1- $\beta$ -D-arabinofuranosylcytosine: synergy of antitumor activity with *cis*-diamminedichloroplatinum(II). *Cancer Res* 1988;**48**:117–21.
41. Fagerberg L, Hallstrom BM, Oksvold P, Kampf C, Djureinovic D, Odeberg J, et al. Analysis of the human tissue-specific expression by genome-wide integration of transcriptomics and antibody-based proteomics. *Mol Cell Proteomics* 2014;**13**:397–406.
42. Mackenzie AE, Milligan G. The emerging pharmacology and function of GPR35 in the nervous system. *Neuropharmacology* 2017;**113**:661–71.
43. Zhao P, Sharir H, Kapur A, Cowan A, Geller EB, Adler MW, et al. Targeting of the orphan receptor GPR35 by pamoic acid: a potent activator of extracellular signal-regulated kinase and  $\beta$ -arrestin2 with antinociceptive activity. *Mol Pharmacol* 2010;**78**:560–8.
44. Widenmaier SB, Snyder NA, Nguyen TB, Arduini A, Lee GY, Arruda AP, et al. NRF1 is an ER membrane sensor that is central to cholesterol homeostasis. *Cell* 2017;**171**:1094–109.
45. Efeyan A, Comb WC, Sabatini DM. Nutrient-sensing mechanisms and pathways. *Nature* 2015;**517**:302–10.
46. Turski MP, Turska M, Paluszkiewicz P, Parada-Turska J, Oxenkrug GF. Kynurenic acid in the digestive system—new facts, new challenges. *Int J Tryptophan Res* 2013;**6**:47–55.
47. Divorty N, Mackenzie AE, Nicklin SA, Milligan G. G protein-coupled receptor 35: an emerging target in inflammatory and cardiovascular disease. *Front Pharmacol* 2015;**6**:41.
48. Milligan G. Orthologue selectivity and ligand bias: translating the pharmacology of GPR35. *Trends Pharmacol Sci* 2011;**32**:317–25.
49. Grada A, Otero-Vinas M, Prieto-Castrillo F, Obagi Z, Falanga V. Research techniques made simple: analysis of collective cell migration using the wound healing assay. *J Invest Dermatol* 2017;**137**:e11–6.
50. Headon D. Reversing stratification during wound healing. *Nat Cell Biol* 2017;**19**:595–7.
51. Gutierrez-Vazquez C, Quintana FJ. Regulation of the immune response by the aryl hydrocarbon receptor. *Immunity* 2018;**48**:19–33.
52. Collins SL, Patterson AD. The gut microbiome: an orchestrator of xenobiotic metabolism. *Acta Pharm Sin B* 2020;**10**:19–32.
53. Kimura A, Naka T, Nakahama T, Chinen I, Masuda K, Nohara K, et al. Aryl hydrocarbon receptor in combination with Stat 1 regulates LPS-induced inflammatory responses. *J Exp Med* 2009;**206**:2027–35.
54. DiNatale BC, Schroeder JC, Perdew GH. Ah receptor antagonism inhibits constitutive and cytokine inducible IL6 production in head and neck tumor cell lines. *Mol Carcinog* 2011;**50**:173–83.
55. DiNatale BC, Schroeder JC, Francey LJ, Kusnadi A, Perdew GH. Mechanistic insights into the events that lead to synergistic induction of interleukin 6 transcription upon activation of the aryl hydrocarbon receptor and inflammatory signaling. *J Biol Chem* 2010;**285**:24388–97.
56. Pulley JM, Rhoads JP, Jerome RN, Challa AP, Erreger KB, Joly MM, et al. Using what we already have: uncovering new drug repurposing strategies in existing omics data. *Annu Rev Pharmacol Toxicol* 2019;**60**:333–52.